Geophysical Journal International

Geophys. J. Int. (2012) **191,** 965–992 doi: 10.1111/j.1365-246X.2012.05665.x

Global 3-D imaging of mantle conductivity based on inversion of observatory *C*-responses—II. Data analysis and results

Alexey Semenov and Alexey Kuvshinov

Institute of Geophysics, ETH Zürich, 8092*, Switzerland. E-mail: asemenov.ch@gmail.com*

Accepted 2012 September 3. Received 2012 June 29; in original form 2011 July 22

SUMMARY

The global 3-D electrical conductivity distribution in the mantle (in the depth range between 400 and 1600 km) is imaged by inverting *C*-responses estimated on a global net of geomagnetic observatories.

Very long time-series (up to 51 years; 1957–2007) of hourly means of three components of the geomagnetic field from 281 geomagnetic observatories are collected and analysed. Special attention is given to data processing in order to obtain unbiased *C*-responses with trustworthy estimates of experimental errors in the period range from 2.9 to 104.2 d. After careful inspection of the obtained *C*-responses the data from 119 observatories are chosen for the further analysis. Squared coherency is used as a main quality indicator to detect (and then to exclude from consideration) observatories with a large noise-to-signal ratio. During this analysis we found that—along with the *C*-responses from high-latitude observatories (geomagnetic latitudes higher than 58°)—the *C*-responses from all low-latitude observatories (geomagnetic latitudes below 11°) also have very low squared coherencies, and thus cannot be used for global induction studies.

We found that the *C*-responses from the selected 119 mid-latitude observatories show a huge variability both in real and imaginary parts, and we investigated to what extent the ocean effect can explain such a scatter. By performing the systematic model calculations we conclude that: (1) the variability due to the ocean effect is substantial, especially at shorter periods, and it is seen for periods up to 40 d or so; (2) the imaginary part of the *C*-responses is to a larger extent influenced by the oceans; (3) two types of anomalous *C*-response behaviour associated with the ocean effect can be distinguished; (4) to accurately reproduce the ocean effect a lateral resolution of $1^\circ \times 1^\circ$ of the conductance distribution is needed, and (5) the ocean effect alone does not explain the whole variability of the observed *C*-responses.

We also detected that part of the variability in the real part of the *C*-responses is due to the auroral effect. In addition we discovered that the auroral effect in the *C*-responses reveals strong longitudinal variability, at least in the Northern Hemisphere. Europe appears to be the region with smallest degree of distortion compared with North America and northern Asia. We found that the imaginary part of the *C*-responses is weakly affected by the auroral source, thus confirming the fact that in the considered period range the electromagnetic (EM) induction from the auroral electrojet is small. Assuming weak dependence of the auroral signals on the Earth's conductivity at considered periods, and longitudinal variability of the auroral effect, we developed a scheme to correct the experimental *C*-responses for this effect.

With these developments and findings in mind we performed a number of regularized 3-D inversions of our experimental data in order to detect robust features in the recovered 3-D conductivity images. Although differing in details, all our 3-D inversions reveal a substantial level of lateral heterogeneity in the mantle at the depths between 410 and 1600 km. Conductivity values vary laterally by more than one order of magnitude between resistive and conductive regions. The maximum lateral variations of the conductivity have been detected in the layer at depths between 670 and 900 km. By comparing our global 3-D results with the results of independent global and semi-global 3-D conductivity studies, we conclude that

3-D conductivity mantle models produced so far are preliminary as different groups obtain disparate results, thus complicating quantitative comparison with seismic tomography or/and geodynamic models. In spite of this, our 3-D EM study and most other 3-D EM studies reveal at least two robust features: reduced conductivity beneath southern Europe and northern Africa, and enhanced conductivity in northeastern China.

Key words: Numerical solutions; Inverse theory; Electrical properties; Geomagnetic induction; Composition of the mantle.

1 INTRODUCTION

Today seismic tomography studies reveal a mantle with a variety of 3-D structures persisting at all length scales (van der Hilst *et al.* 1991; Grand 1994; Helffrich & Wood 2001; Becker & Boschi 2002, among others), providing evidence of the complex dynamics that have shaped mantle structure. In spite of many advances, seismology is yet to provide a clear picture of the origin of the large-scale heterogeneities (Helffrich & Wood 2001).

An alternative means of addressing mantle heterogeneity is to investigate properties that in principle are more sensitive to parameters such as composition, temperature and water content than elasticity. One such property is electrical conductivity, and electromagnetic (EM) imaging based on this property presents an intriguing prospect for unraveling the nature of mantle heterogeneous structures. Lateral variations in conductivity have been reported in a number of regional 1-D EM studies (Schultz & Larsen 1987; Egbert *et al.* 1992; Lizarralde *et al.* 1995; Neal *et al.* 2000; Fukao *et al.* 2004; Tarits *et al.* 2004; Jones *et al.* 2009; Khan *et al.* 2011, among others) as well as in the first global and semi-global 3-D EM inversions (Fukao *et al.* 2004; Koyama *et al.* 2006; Kelbert *et al.* 2009; Utada *et al.* 2009; Shimizu *et al.* 2010b) based on analysis of observatory *C*-responses. The interested reader is referred to the paper by Kuvshinov (2012) where the progress in the past 10 years in deep geomagnetic studies is summarized.

In this paper we continue the effort of retrieving information on the global 3-D mantle conductivity distribution. We pay particular attention to data analysis, as the procurement of a set of internally consistent and coherent response functions is singularly important. Two—ocean and auroral—effects are addressed in a systematic way in an attempt to understand quantitatively their distorting influence on the responses.

The content of the paper is as follows. Section 2 describes the estimation and analysis of a new set of *C*-responses. Our aim was to obtain reliable *C*-responses which cover the broadest possible period range from the largest possible number of observatories. In Sections 3 and 4 we investigate to what extent ocean and auroral effects can explain huge variability of the responses, and develop schemes to correct the observed responses for these two effects. In Section 5 we present the results of our 3-D inversions and compare them with the results of independent studies. To detect robust features in the conductivity images we perform three 3-D inversion runs which differ by an amount of the corrections is applied to the data. In the first run data are not corrected neither for ocean nor for auroral effects. In the second run we correct the data for the auroral effect. Finally, in the third run we invert the data corrected both for ocean and auroral effects. The 3-D inverse solution itself is explained in a companion paper by Kuvshinov & Semenov (2012). Section 6 contains conclusions and suggests topics for future work.

2 DATA ANALYSIS

2.1 Data collection

We assembled very long time-series (up to 51 years; 1957–2007) of hourly mean values of three components of the geomagnetic field from 281 geomagnetic observatories, including polar and equatorial observatories. These data were retrieved from the Edinburgh World Data Center for Geomagnetism (http://www.wdc.bgs.ac.uk). The spatial distribution of observatories is shown in Fig. 1.

We first visually inspected all the data and found that very few observatories (mostly in Europe and Japan) provide continuous time-series of good quality (without baseline jumps and gaps) for the whole 51-year interval. As an example the left-hand plot in Fig. 2 shows time-series of the geomagnetic field components for one of the best (with respect to data quality) observatories—Hermanus (HER) in South Africa. Data found to have gaps and/or involve baseline jumps were excluded. No attempt has been made to edit the data. This decision is motivated by the intention to avoid any uncertainties associated with the necessarily subjective editing schemes. Our hope was that by using very long time-series the above simple criteria would provide enough data for further analysis. The right-hand plot in Fig. 2 demonstrates the data of 'moderate' quality from the Chinese observatory Sheshan (SSH). In spite of clear baseline jumps and lengthy gaps in the data, time intervals of considerable duration showing continuous observations without jumps and outliers are nonetheless extant. Note that usable data from many observatories exist only for periods of as little as a few months down to a few days (e.g. EIC, Easter Island in the Pacific Ocean), preventing their use. After the initial processing step data from 262 observatories remained. Based on the results of time-series analysis, to be discussed below, we further decreased more than twice this subset of observatories.

2.2 Determination of *C*-responses

In this section we discuss details of time-series analysis to estimate *C*-responses, which we write here in the following form (Banks 1969)

$$C(\mathbf{r}_a, \omega) = -\frac{a \tan \vartheta}{2} \frac{Z(\mathbf{r}_a, \omega)}{H(\mathbf{r}_a, \omega)}, \quad (1)$$

where $Z \equiv -B_r$ and $H \equiv -B_\vartheta$, a is the mean Earth's radius, and ϑ is the geomagnetic colatitude.

This technique of estimation and analysis of *C*-responses will be referred to below as the geomagnetic depth sounding (GDS) method.

2.2.1 Least-squares approach

The procedure presented below describes how we estimated *C*-responses.

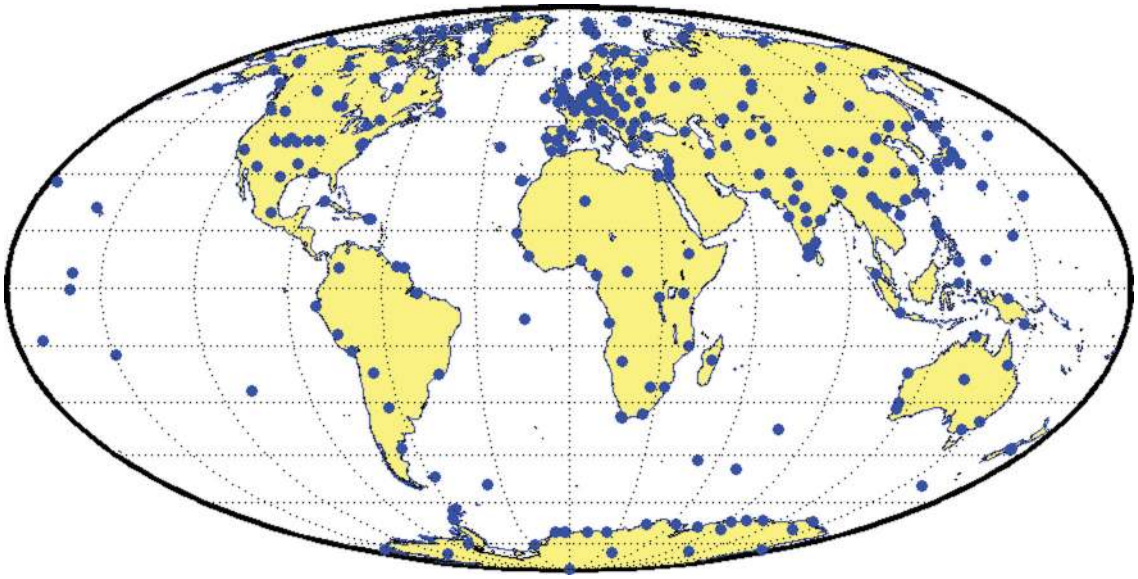

Figure 1. Location of 281 observatories, data from which have been retrieved from Edinburgh World Data Center for Geomagnetism.

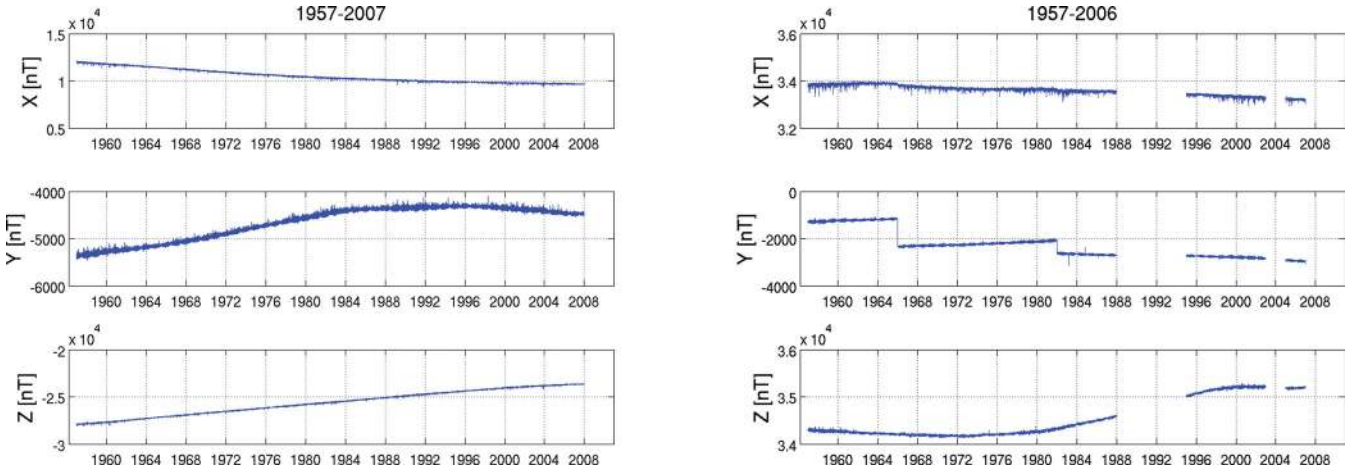

Figure 2. Time-series of hourly mean values of *X, Y* and *Z* components of the magnetic field at Hermanus (HER) observatory (left) in South Africa and at Sheshan (SSH) observatory (right) in China.

(1) Secular variation is removed from the original time-series. For each component the secular variation is treated by means of cubic B-splines with a knot separation of 2 yr.

(2) The resulting time-series of the horizontal component are transformed by a rotation from a geographic to a geomagnetic (dipolar) coordinate system. Location of the geomagnetic pole has been obtained from dipole components of the IGRF 1985 model. The secular motion of the pole is not relevant because this rate is much slower than the period range of interest.

(3) Segments of Z and H time-series of length KT_j (hereinafter referred to as realizations) are taken for estimating time harmonics of Z and H at various periods $T_j, j = 1, \ldots, N_T$, with N_T being the number of considered periods and K being a constant. The responses were estimated on 15 periods between 2.9 and 104.2 d, evenly spaced on a logarithmic scale. There is a consensus that the GDS method works well in this period range (*cf.* Banks 1969; Roberts 1984; Schultz & Larsen 1987; Fujii & Schultz 2002, among others). We varied K between 3 and 10 and finally choose $K = 7$, considering this value as a good compromise between resolution and accuracy of the response estimates. In order to increase the number of realizations, successive realizations overlap 50 per cent with preceding ones. If a given realization contains gaps in either component (Z or H), we exclude it from further analysis. To reduce sidelobes a Kaiser window (Kuo & Kaiser 1966) is applied to each realization. This window is an approximation to the prolate-spheroidal window, for which the ratio of the main lobe energy to the side lobe energy is maximized.

(4) For each realization and for each period T_j, we calculate a frequency-dependent $\hat{Z}_l$ and $\hat{H}_l$ using the Fourier transform

$$\hat{Z}_l(\omega_j) = \int_{t_l}^{t_l+KT_j} S(t)Z(t)\mathrm{e}^{-\mathrm{i}\omega_j t}\,\mathrm{d}t,$$
$$\hat{H}_l(\omega_j) = \int_{t_l}^{t_l+KT_j} S(t)H(t)\mathrm{e}^{-\mathrm{i}\omega_j t}\,\mathrm{d}t, \qquad (2)$$

where $l = 1, \ldots, L$, L is the number of realizations S is a function which describes the Kaiser window, and t_l is the first time instant of the realization. Hereinafter we will use the symbols Z and H for frequency-dependent fields in place of $\hat{Z}$ and $\hat{H}$.

(5) Least-squares C-responses are then estimated as

$$C = -\frac{a\tan\vartheta}{2}\frac{\langle ZWH^*\rangle}{\langle HWH^*\rangle}, \tag{3}$$

where H^* is the complex conjugate of H, and $\langle\cdots\rangle$ denotes summation over the L realizations

$$\langle AWH^*\rangle = \sum_{l=1}^{L} A_l W_l H_l^*, \tag{4}$$

where A is either Z or H. Non-Gaussian noise is handled with an iterative robust (Huber) weight W, which reduces the effect of outliers (Huber 1981). The corresponding errors are calculated as follows (Schmucker 1999):

$$\delta C(\omega) = |C|\sqrt{\frac{1-\mathrm{coh}^2}{\mathrm{coh}^2}\left(\frac{1}{\beta}\right)^{\frac{1}{L-1}}}, \tag{5}$$

where $1-\beta$ is the confidence level, i.e. probability that the absolute value $|C|$ lies within error limits $|C| \pm \delta C$. In our calculations the confidence level is chosen to be 0.9. Squared coherence coh^2 is calculated as

$$\mathrm{coh}^2 = \frac{|\langle ZWH^*\rangle|^2}{\langle ZWZ^*\rangle\langle HWH^*\rangle}. \tag{6}$$

In Section 2.2.3 the squared coherence will be used as the quality indicator, which allows for detecting sites with large noise-to-signal ratios. Let us provide the reasonings for this decision. Following Olsen (1998) we denote true signals of magnetospheric origin (for each realization l) as $Z_{0,l}$ and $H_{0,l}$, and noise parts in Z_l and H_l as δZ_l and δH_l:

$$\begin{aligned} Z_l &= Z_{0,l} + \delta Z_l, \\ H_l &= H_{0,l} + \delta H_l. \end{aligned} \tag{7}$$

Eq. (1) should then be written as

$$C = -\frac{a\tan\vartheta}{2}\frac{Z_{0,l}+\delta Z_l}{H_{0,l}+\delta H_l}, \tag{8}$$

where $Z_{0,l}$ and $H_{0,l}$ are assumed to be exactly correlated:

$$-\frac{a\tan\vartheta}{2}Z_{0,l} = E(C)H_{0,l}. \tag{9}$$

Here $E(C)$ denotes the expected value for C. Let us further assume that

$$\begin{aligned} \langle\delta HW\delta Z^*\rangle &= \langle\delta ZWZ_0^*\rangle = \langle\delta HWH_0^*\rangle = \langle\delta ZWH_0^*\rangle \\ &= \langle\delta HWZ_0^*\rangle = 0. \end{aligned} \tag{10}$$

Then eq. (6) can be rewritten as

$$\begin{aligned} \mathrm{coh}^2 &= \frac{|\langle ZWH^*\rangle|^2}{\langle ZWZ^*\rangle\langle HWH^*\rangle} = \frac{\langle ZWH^*\rangle}{\langle ZWZ^*\rangle}\frac{\langle HWZ^*\rangle}{\langle HWH^*\rangle} \\ &= \frac{\langle Z_0WH_0^*\rangle}{\langle Z_0WZ_0^*\rangle + \langle\delta ZW\delta Z^*\rangle}\frac{\langle H_0WZ_0^*\rangle}{\langle H_0WH_0^*\rangle + \langle\delta HW\delta H^*\rangle} \\ &= \frac{\langle Z_0WH_0^*\rangle}{\langle Z_0WZ_0^*\rangle}\frac{1}{\left(1+\frac{\langle\delta ZW\delta Z^*\rangle}{\langle Z_0WZ_0^*\rangle}\right)}\frac{\langle H_0WZ_0^*\rangle}{\langle H_0WH_0^*\rangle}\frac{1}{\left(1+\frac{\langle\delta HW\delta H^*\rangle}{\langle H_0WH_0^*\rangle}\right)} \\ &= \frac{1}{\left(1+\frac{\langle\delta ZW\delta Z^*\rangle}{\langle Z_0WZ_0^*\rangle}\right)\left(1+\frac{\langle\delta HW\delta H^*\rangle}{\langle H_0WH_0^*\rangle}\right)}, \end{aligned} \tag{11}$$

where we have made use of the equality

$$\frac{\langle Z_0WH_0^*\rangle}{\langle Z_0WZ_0^*\rangle} = \frac{\langle H_0WH_0^*\rangle}{\langle H_0WZ_0^*\rangle}, \tag{12}$$

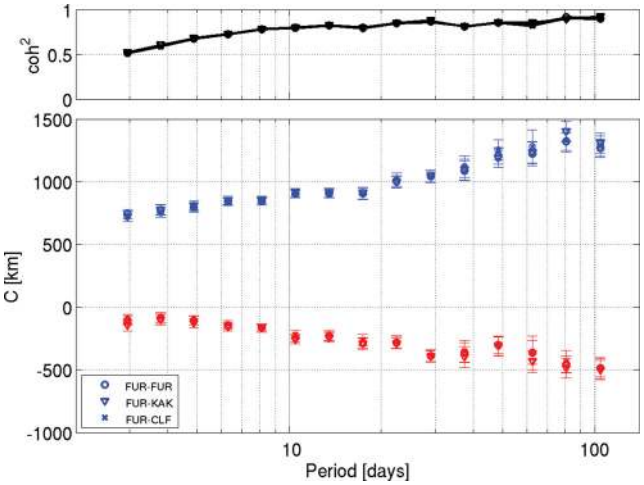

Figure 3. C-responses for Fürstenfeldbruck observatory estimated with the use of eqs (3) and (13) (for details see the text). Circles signify the results obtained from 'single site' estimation (using eq. 3), triangles and crosses denote the results obtained using remote reference technique (see eq. 13) with Kakioka (KAK) and Chambon-la-Forêt (CLF) as respective reference observatories. In the most figures of the paper which show the responses blue and red colours are reserved for real and imaginary parts of the C-responses, respectively.

which arises from the exact correlation of Z_0 and H_0 (see eq. 9). It is seen from eq. (11) that low squared coherence means high relative errors in Z or/and in H. These errors are possible due to a combination of the following cases: (1) instrumental or/and environmental noise; (2) smallness of the true signal, and (3) violation of the assumption about P_1^0 structure of the true signal. With regard to the use of eq. (3) for estimating C-responses, the question of a possible downward bias of the responses arises (Olsen 1998). In order to address this issue, we calculate responses using the remote reference technique (Gamble *et al.* 1979), which allows for a reduction of downward bias of the C-response estimates (should this bias exist). Using this technique the responses are computed as follows:

$$C = -\frac{a\tan\vartheta}{2}\frac{\langle ZWH_{\mathrm{ref}}^*\rangle}{\langle HWH_{\mathrm{ref}}^*\rangle}, \tag{13}$$

where H_{ref} are realizations at the reference observatory, which is sufficiently far away so that the noise sources in H and H_{ref} are independent. Applying this technique we found that estimates calculated with the use of eqs (3) and (13) are very similar for all observatories over the period range of interest. We paired the observatories with different remote reference observatories, but noticed only a negligible difference between the different estimates so computed. This is illustrated in Fig. 3, which shows the results of C-response estimates for FUR estimated with the use of eqs (3) and (13). Circles depict the results obtained from 'single site' estimation (i.e. using eq. 3; triangles and crosses denote the results obtained using the remote reference technique, see eq. 13), employing Kakioka (KAK) observatory in Japan and Chambon-la-Forêt (CLF) in France as remote reference observatories. The responses are seen to be very close over the whole period range, which means that the use of eq. (3) for obtaining unbiased estimates of C-responses seems adequate.

2.2.2 *The jackknife method*

We also applied an alternative (jackknife) method (*cf.* Chave & Thomson 1989) to estimate C-responses and their uncertainties.

The advantage of the jackknife method over the least-squares approach discussed earlier is twofold. First, jackknife estimates of the responses tend to be bias-free (see Efron 1982). Secondly, the jackknife method does not require assumptions about the statistical distribution of experimental errors and, thus, gives a more realistic estimate of the response uncertainties. The method works as follows. Let us designate

$$\langle AWH^*\rangle_i = \sum_{j=1}^{i-1} A_j W_j H_j^* + \sum_{j=i+1}^{L} A_j W_j H_j^*, \tag{14}$$

and

$$\hat{C}_i = \frac{\langle ZWH^*\rangle_i}{\langle HWH^*\rangle_i}. \tag{15}$$

Then the jackknife estimate of the response, $\tilde{C}$, is determined as

$$\tilde{C} = L\hat{C} - \frac{(L-1)}{L}\sum_{i=0}^{N}\hat{C}_i, \tag{16}$$

where $\hat{C}$ is calculated as in eq. (3) from all available (L) realizations. The jackknife estimate of the variance is written as

$$\tilde{s}^2 = \frac{L-1}{L}\sum_{i=1}^{L}\left|\hat{C}_i - \frac{1}{L}\sum_{j=1}^{L}\hat{C}_j\right|^2. \tag{17}$$

Under very general conditions, it can be shown (*cf.* Chave & Thomson 1989) that $\frac{\tilde{C}-C}{\tilde{s}}$ is asymptotically normally distributed, allowing the exact value of C with probability $1-\gamma$ to be placed between

$$\tilde{C} - t_\nu\left(1-\frac{\gamma}{2}\right)\tilde{s} \le C \le \tilde{C} + t_\nu\left(1-\frac{\gamma}{2}\right)\tilde{s}, \tag{18}$$

where $t_\nu(1-\frac{\gamma}{2})$ is a value from Student's distribution with ν degrees of freedom. In our calculations we took $\gamma = 0.1$. Thus, within the jackknife approach we can estimate uncertainty, dC, as

$$\mathrm{d}C = t_\nu\left(1-\frac{\gamma}{2}\right)\tilde{s}. \tag{19}$$

Fig. 4 presents comparison of estimates of C-responses and their uncertainties obtained by the least-squares and the jackknife methods. The results are presented for the observatory Alice Springs (ASP) in Australia and the observatory Hermanus. It is seen from the figure that the two methods give comparable estimates, both of responses and uncertainties. These model studies demonstrate that we are rather safe by using either least-squares or jackknife methods, however we prepared the final set of C-responses and their uncertainties with the use of the jackknife scheme.

2.2.3 C-responses' selection

As previously mentioned the (squared) coherency can serve as a proxy either for estimating the quality of the responses at a given observatory, or/and for detecting observatories where the assumption of a P_1^0 source structure is violated. Fig. 5 quantitatively summarizes information in a form of coherencies at 262 observatories. The upper plot in Fig. 5 presents this information in a form of global map where the circles of different sizes stand for the averaged [over all (15) periods] coherencies at a given observatory. The lower plot shows the same averaged coherencies versus geomagnetic latitude. It is clearly seen from the figure that the coherence dramatically drops at geomagnetic latitudes higher than 58° and below 11° [these latitudes are depicted in the plots by solid (upper plot) and dotted (lower plot) lines].

The decrease in coherency is particularly prominent in the vicinity of the geomagnetic equator, which is likely due to the assumed geometry of the magnetospheric source. For this source (described by the first zonal harmonic, $P_1^0 = \cos\vartheta$, in geomagnetic coordinates) the vertical component, Z, near geomagnetic equator tends to 0, thus enlarging the noise-to-signal ratio, as a consequence of which coherency diminishes (see eq. 11). As a result, the GDS method fails in this region as is illustrated in the left-hand plot of Fig. 6, showing C-responses, uncertainties and coherencies for the equatorial observatory Guam (GUA; geomagnetic (GM) latitude, $\vartheta = 5°$N; North Pacific). Indeed, along with the low squared coherency, C-responses are seen to be very scattered and have large uncertainties.

Coherency at high-latitude observatories is also very low, which is explained by the fact that in this region the main source of the magnetic field variations is the ionospheric polar electrojet. This source has spatial structure that is very different from the here-assumed P_1^0 structure of our magnetospheric source, which thus prevents us from implementing the GDS method at high latitudes. The right-hand plot in Fig. 6 shows the results for the high-latitude observatory Sitka (SIT; $\vartheta = 60°$N; Alaska) and supports this inference. Here the responses have unphysical values (e.g. real parts of

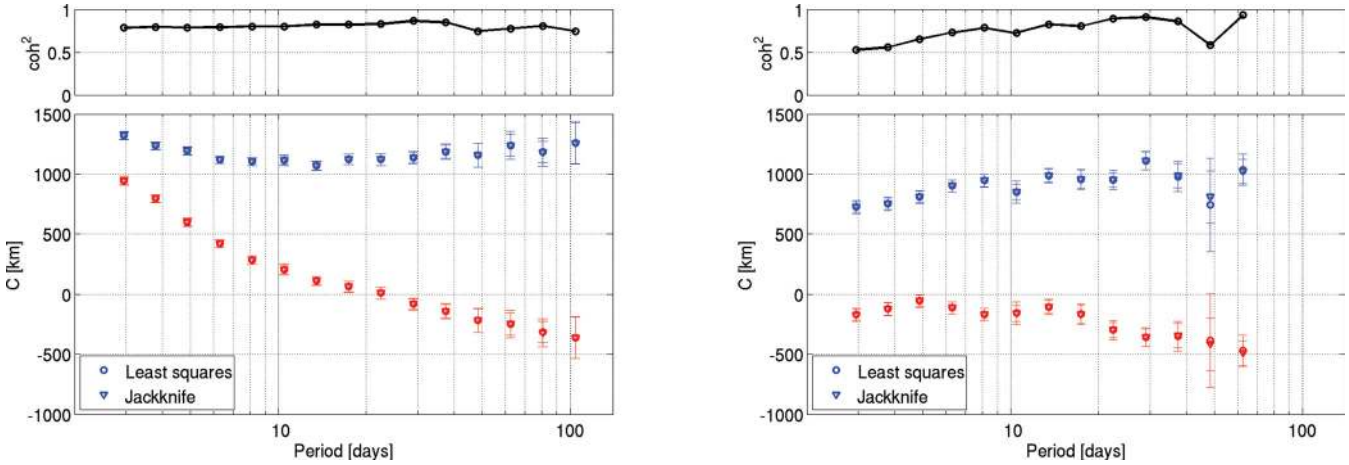

Figure 4. Comparison of least-squares and jackknife techniques used to calculate C-responses on the Hermanus observatory (left-hand plot) and the Alice Springs observatory in Australia (right-hand plot).

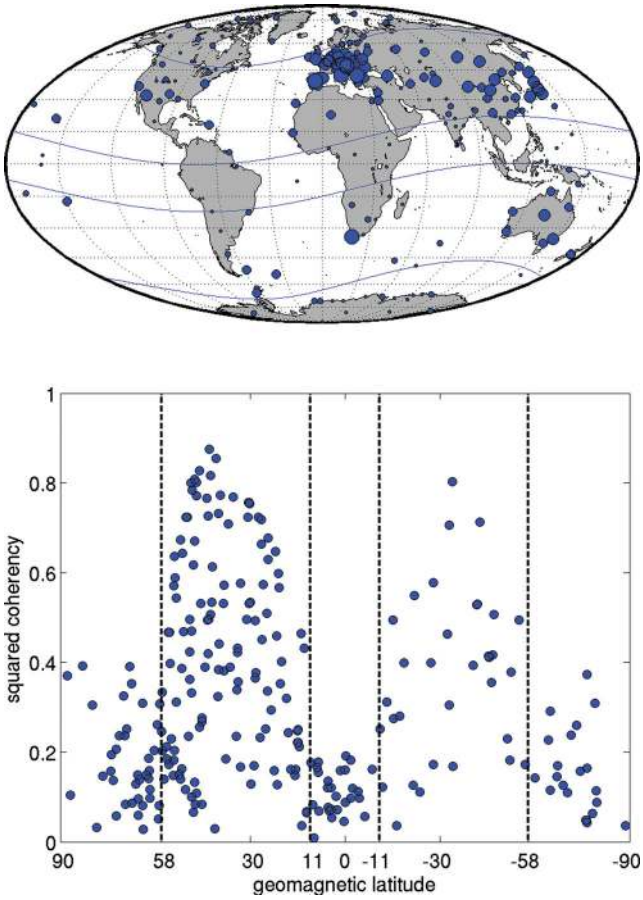

Figure 5. Averaged over all periods squared coherencies at 262 pre-selected observatories. Upper plot shows averaged coherency at a given observatory, where the circles stand for averaged coherencies; the larger the size of the circle the higher the coherency (five different sizes correspond to the following intervals: 0–0.2; 0.2–0.4; 0.4–0.6; 0.6–0.8, 0.8–1). Lower plot presents the distribution of the averaged coherency with respect to geomagnetic latitude.

C-responses are negative for most of the periods) and the coherency between *Z* and *H* signals is very low.

Applying these additional constraints, *C*-responses from 119 mid-latitude observatories remained for further analysis. Fig. 7

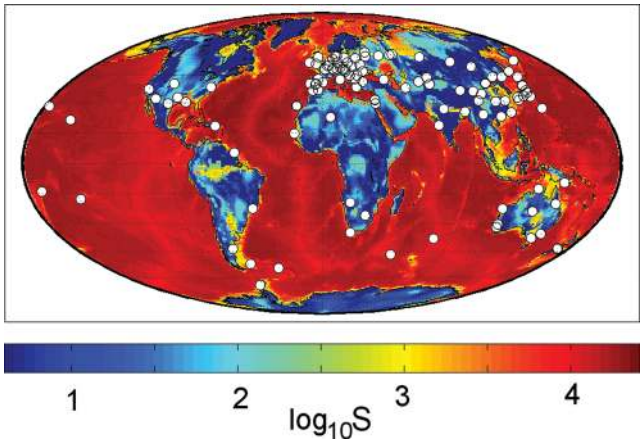

Figure 7. Conductance map using a logarithmic scale. Location of the 119 mid-latitude observatories employed during 3-D inversion are shown as white dots.

shows the location of the selected observatories and the surface conductance map, which describes the non-uniform distribution of the conductive oceans and resistive continents. Table 1 summarizes station details such as their acronyms, names, locations (both in geographic and GM coordinates) and time interval used for estimating *C*-responses.

In Fig. 8 we show the variability of the selected *C*-responses of both real and imaginary parts. Black circles in these plots show the responses that have been calculated from the global 1-D conductivity profile, derived from five years of satellite (CHAMP, Orsted and SAC-C) magnetic data by Kuvshinov & Olsen (2006). One can see that the observed responses show a huge variability both in real and imaginary parts, and in the next section we investigate to what extent the variability of our collection of the experimental responses can be understood by the ocean effect. We would also like to know how the ocean effect shows up in the responses in different regions of the world.

3 OCEAN EFFECT REVISITED

There is a common understanding that two 3-D induction effects prevail in the responses: those caused by the distribution of land and sea, and those due to the heterogeneous mantle. Kuvshinov

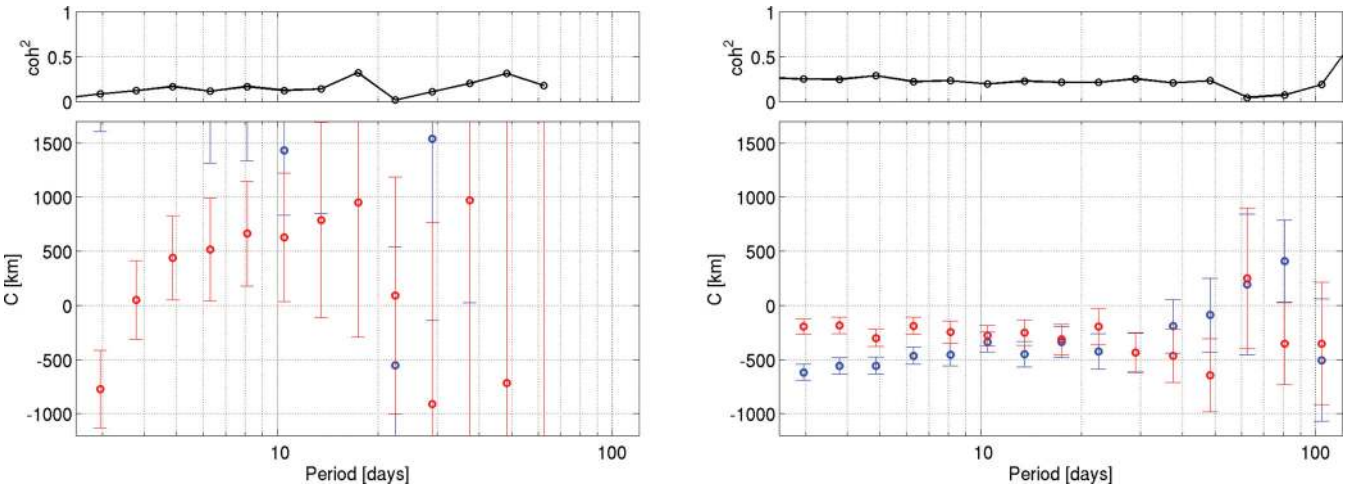

Figure 6. Left: *C*-responses at equatorial observatory Guam (GUA) in the Pacific Ocean (5°N GM). Right: *C*-responses at high-latitude observatory Sitka (SIT) in Alaska (60°N GM).

Table 1. Station details: acronyms, names, locations (both in geographic and geomagnetic coordinates) and time interval for estimating *C*-responses. The last column provides information in which cluster the station belongs (see details in Section 3.4 describing ocean effect).

Code	Station	Latitude	Longitude	GM Latitude	GM Longitude	Data length	Cluster
AAA	Alma Ata	43.250	76.920	34.29	152.74	1963-2007	CN
ABG	Alibag	18.638	72.872	10.19	146.16	1957-2007	CN
AIA	Faraday Islands	−65.250	295.730	−55.06	5.49	1957-2007	SA
ALM	Almeria	36.853	357.540	39.83	77.12	1957-1966	EU
AML	Amberley	−43.152	172.722	−46.80	254.13	1961-1977	AU
AMS	Martin de Vivies	−37.796	77.574	−46.39	144.27	1981-2007	AU
AMT	Amatsia	31.550	34.917	28.12	112.26	1979-2000	EU
API	Apia	−13.807	188.225	−15.36	262.65	1957-2007	AU
AQU	L'Aquila	42.383	13.317	42.42	94.50	1960-2007	EU
ARS	Arti	56.433	58.967	49.13	139.91	1973-2007	EU
ASH	Vannovskaya	37.950	58.100	31.01	135.09	1972-1990	EU
ASO	Aso	32.882	131.009	23.35	200.75	1957-1959	CN
ASP	Alice Springs	−23.761	133.883	−32.91	208.18	1992-2007	AU
BDV	Budkov	49.080	14.015	48.97	97.61	1994-2007	EU
BEL	Belsk	51.837	20.792	50.24	105.17	1966-2007	EU
BFE	Brorfelde	55.625	11.672	55.45	98.48	1981-2007	EU
BFO	Black Forest	48.330	8.320	49.06	91.80	2006-2007	EU
BGY	Bar Gyora	31.723	35.088	28.26	112.46	2003-2007	EU
BJI	Beijing	40.040	116.175	29.87	187.02	1960-1980	CN
BMT	Beijing Ming Tombs	40.300	116.200	30.13	187.04	1996-2007	CN
BOU	Boulder	40.130	254.760	48.40	320.59	1967-2007	NA
BOX	Borok	58.070	38.230	53.41	123.52	1980-2007	EU
BSL	Bay St. Louis	30.350	270.370	40.05	339.79	1986-2007	NA
CBI	Chichijima	27.096	142.185	18.47	211.63	1991-2006	CN
CDP	Chengdu	31.000	103.700	20.77	175.86	1995-2007	CN
CLF	Chambon-la-Foret	48.025	2.261	49.84	85.68	1957-2007	EU
CNB	Canberra	−35.315	149.363	−42.71	226.94	1979-2007	AU
CNH	Changchun	43.827	125.299	33.96	194.80	1979-2007	CN
COI	Coimbra	40.220	351.580	44.14	71.99	1992-1994	EU
CTA	Charters Towers	−20.090	146.264	−28.01	220.97	1990-2007	AU
CZT	Port Alfred	−46.431	51.867	−51.35	113.28	1982-2007	SA
DAL	Dallas	32.980	263.250	42.15	331.47	1964-1974	NA
DLR	Del Rio	29.490	259.080	38.30	327.31	1982-2007	NA
DOU	Dourbes	50.100	4.600	51.43	88.90	1957-2007	EU
EBR	Ebro	40.821	0.493	43.18	81.30	1957-2007	EU
ELT	Eilat	29.670	34.950	26.27	111.89	1998-2007	EU
ESA	Esashi	39.237	141.355	30.46	209.42	2000-2007	CN
ESK	Eskdalemuir	55.317	356.800	57.80	83.75	1957-2007	EU
EYR	Eyrewell	−43.410	172.350	−47.11	253.83	1978-2007	AU
FRD	Fredericksburg	38.200	282.630	48.40	353.38	1957-2007	NA
FRN	Fresno	37.090	240.280	43.52	305.25	1982-2007	NA
FUR	Furstenfeldbruck	48.165	11.277	48.38	94.61	1957-2007	EU
GCK	Grocka	44.633	20.767	43.29	102.40	1965-2007	EU
GLM	Golmud	36.400	94.900	26.39	168.06	1995-2006	CN
GNA	Gnangara	−31.780	115.947	−41.93	188.84	1957-2007	AU
GUI	Guimar	28.321	343.559	33.78	60.59	1993-2007	EU
GZH	Guangzhou	23.093	113.343	12.88	184.84	1960-2007	CN
HAD	Hartland	51.000	355.517	53.90	80.17	1957-2007	EU
HBK	Hartebeesthoek	−25.883	27.707	−27.13	94.40	1972-2007	SA
HER	Hermanus	−34.425	19.225	−33.98	84.02	1957-2007	SA
HLP	Hel	54.608	18.817	53.24	104.63	1966-2007	EU
HON	Honolulu	21.320	202.000	21.64	269.74	1961-2007	NP
HRB	Hurbanovo	47.873	18.190	46.87	101.11	1957-2007	EU
HTY	Hatizyo	33.073	139.825	24.20	208.98	1986-2005	CN
IRT	Irkutsk	52.167	104.450	41.93	176.90	1957-2007	CN
ISK	Istanbul Kandilli	41.063	29.062	38.40	109.11	1957-1999	EU
JAI	Jaipur	26.920	78.900	17.92	152.32	1979-1987	CN
KAK	Kakioka	36.232	140.186	27.37	208.95	1957-2007	CN
KDU	Kakadu	−12.686	132.472	−21.99	205.61	1995-2007	AU
KIV	Kiev	50.720	30.300	47.57	113.43	1958-1991	EU
KNY	Kanoya	31.424	130.880	21.89	200.75	1958-2006	CN
KNZ	Kanozan	35.256	139.956	26.38	208.65	1980-2007	CN

Table 1. (*Continued.*)

Code	Station	Latitude	Longitude	GM Latitude	GM Longitude	Data length	Cluster
KZN	Kazan	55.830	48.850	49.75	131.59	1978-1989	EU
KOU	Kourou	5.210	307.269	14.89	19.66	1996-2007	NA
KSH	Kashi	39.500	76.000	30.64	151.44	1995-2007	CN
LGR	Logrono	42.450	357.500	45.29	78.80	1963-1966	EU
LNP	Lunping	25.000	121.167	14.99	192.14	1965-2007	CN
LRM	Learmonth	−22.222	114.101	−32.42	186.46	1990-2007	AU
LVV	Lviv	49.900	23.750	47.87	107.11	1957-2007	EU
LZH	Lanzhou	36.087	103.845	25.86	176.08	1980-2007	CN
MAB	Manhay	50.300	5.680	51.42	90.05	1995-2007	EU
MBO	Mbour	14.384	343.033	20.11	57.47	1957-2007	EU
MID	Midway	28.210	182.620	25.02	249.50	2000-2002	NP
MIZ	Mizusawa	39.112	141.204	30.32	209.30	2000-2007	CN
MMB	Memambetsu	43.910	144.189	35.35	211.26	1957-2007	CN
MNK	Pleshenitzi(Minsk)	54.500	27.883	51.60	112.82	1961-1994	EU
MOS	Moscow	55.467	37.312	51.04	121.57	1957-2005	EU
MZL	Manzhouli	49.600	117.400	39.45	187.70	1995-2007	CN
NCK	Nagycenk	47.633	16.717	46.90	99.62	1993-2007	EU
NGK	Niemegk	52.072	12.675	51.88	97.64	1957-2007	EU
NVS	Novosibirsk	55.030	82.900	45.57	159.51	1966-2007	CN
ODE	Odessa	46.780	30.880	43.66	112.55	1957-1991	EU
PAG	Panagyurishte	42.520	24.180	40.65	104.95	1964-2007	EU
PEG	Penteli	38.083	23.933	36.37	103.43	1999-2003	EU
PET	Paratunka	53.100	158.630	45.95	221.73	1969-1995	NP
PMG	Port Moresby	−9.460	147.160	−17.36	220.51	1958-1991	AU
PPT	Pamatai	−17.567	210.426	−15.14	285.14	1968-1994	AU
PST	Port Stanley	−51.703	302.110	−41.69	11.50	1994-2007	SA
QIX	Qianling	34.600	108.200	24.34	179.99	1995-2006	CN
RSV	Rude Skov	55.483	12.457	55.18	99.14	1957-1980	EU
SFS	San Fernando	36.462	353.795	40.09	73.18	1995-2004	EU
SGE	South Georgia	−54.280	323.520	−45.57	28.81	1975-1982	SA
SHL	Shillong	25.550	91.880	15.68	164.72	1976-1987	CN
SJG	San Juan	18.110	293.850	28.31	6.08	1967-1982	NA
SPT	San Pablo	39.547	355.651	42.78	75.98	1997-2007	EU
SSH	Sheshan	31.097	121.187	21.08	191.89	1983-2006	CN
SSO	Simosato	33.575	135.940	24.39	205.19	1957-1965	CN
SUA	Surlari	44.680	26.253	42.39	107.58	1994-2007	EU
SVD	Ekaterinburg	56.730	61.070	49.14	142.07	1957-1980	CN
TAM	Tamanrasset	22.792	5.530	24.66	81.76	1993-2007	EU
TEN	Las Mesas	28.480	343.740	33.91	60.82	1973-1992	EU
TFS	Tbilisi	42.080	44.700	36.91	123.82	1957-2001	EU
THJ	Tonghai	24.000	102.700	13.79	174.81	1995-2007	CN
THY	Tihany	46.900	17.900	45.99	100.47	1957-2007	EU
TKT	Tashkent	41.333	69.617	33.05	146.02	1975-1981	CN
TOL	Toledo	39.880	355.950	43.06	76.39	1957-1980	EU
TOO	Toolangi	−37.530	145.470	−45.38	223.12	1957-1979	AU
TRW	Trelew	−43.248	294.685	−33.05	5.62	1957-2007	SA
TSU	Tsumeb	−19.202	17.584	−18.97	85.83	1964-2007	SA
TUC	Tucson	32.170	249.270	39.88	316.11	1957-1994	NA
VAL	Valentia	51.930	349.750	55.79	74.63	1957-2007	EU
VLA	Gornotayezhnaya	43.683	132.167	34.19	200.79	1958-1988	CN
VSS	Vassouras	−22.400	316.350	−13.29	26.61	2000-2007	SA
WAT	Watheroo	−30.318	115.877	−40.47	188.90	1957-1958	AU
WHN	Wuhan	30.528	114.559	20.33	185.82	2000-2007	EU
WIK	Wien Kobenzl	48.265	16.318	47.58	99.49	1957-1984	EU
WIT	Witteveen	52.813	6.668	53.66	92.20	1957-1984	EU
WNG	Wingst	53.743	9.073	54.12	95.00	1957-2007	EU
YSS	Yuzhno Sakhalinsk	46.950	142.717	38.24	209.49	1970-1988	CN

et al. (2002) demonstrated that up to periods of 20 d a non-uniform ocean is a major contributor to the anomalous behaviour of the *C*-responses at coastal observatories. This was concluded by comparing predicted (in the model with non-uniform oceans) and observed responses at five coastal geomagnetic observatories: Apia (South Pacific), Hermanus (South Africa), Kakioka, Kanoya and Simosato (all in Japan). The authors also concluded that in order to achieve good agreement between predictions and observations one needs: (1) good lateral resolution of the conductance distribution (grid with a lateral resolution of $2^\circ \times 2^\circ$ or denser); and (2) highly

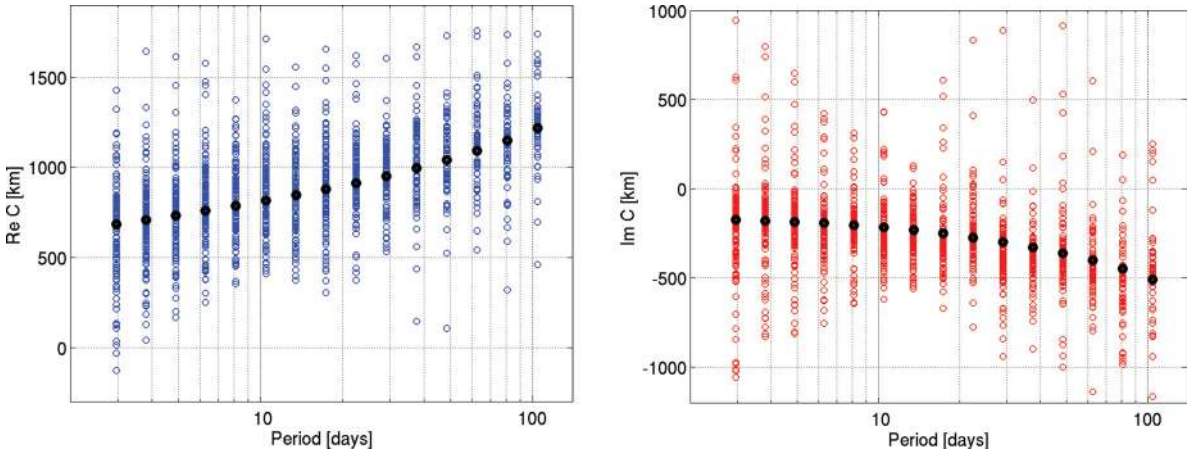

Figure 8. The variability of the real (left) and imaginary (right) parts of experimental responses at selected observatories. Hereinafter in figures black circles show the responses which have been calculated from the global 1-D conductivity profile, derived from five years of satellite (CHAMP, Orsted, and SAC-C) magnetic data by Kuvshinov & Olsen (2006).

resistive lithosphere. Kuvshinov *et al.* (2002) also showed that the effects arising from the oceans may be corrected for by multiplying the observed response, $C^{\rm exp}$, by the ratio of the synthetic response of a radially symmetric conductive earth (without oceans), C^{1D}, with the response of the same radially symmetric conductive earth overlain by an inhomogeneous shell (shell approximates the non-uniform oceans), $C^{1D\ +\rm shell:}$,

$$C^{\rm exp,corr}(\omega) = C^{\rm exp}(\omega) \times \frac{C^{1D}(\omega)}{C^{1D+\rm shell}(\omega)}. \qquad (20)$$

In this section we analyse the ocean effect in the responses from all 119 observatories that we selected for further analysis. The 3-D ('ocean+1-D') model, which is used to predict the ocean effect, consists of a thin spherical layer of laterally varying surface conductance $S(\vartheta, \varphi)$ (see conductance distribution in Fig. 7) and a radially symmetric conductivity $\sigma(r)$ underneath. The shell conductance $S(\vartheta, \varphi)$ is obtained by considering contributions from both sea water and from sediments. The conductance of sea water is taken from Manoj *et al.* (2006), which accounts for ocean bathymetry (taken from the global $5' \times 5'$ NOAA ETOPO map of bathymetry/topography), ocean salinity, temperature and pressure (taken from the World Ocean Atlas 2001). Conductance of the sediments (in continental as well as oceanic regions) is based on the global sediment thicknesses given by the $1^\circ \times 1^\circ$ map of Laske & Masters (1997) and calculated by a heuristic procedure similar to that described by Everett *et al.* (2003). The underlying radially symmetric (1-D) conductivity model, $\sigma(r)$, includes a 100 km resistive lithosphere of 3000 Ohm-m and a layered model underneath derived by Kuvshinov & Olsen (2006).

3.1 Resolution studies

We first investigate what lateral resolution of the model is needed to adequately represent the ocean effect. We calculated the responses for the selected 119 observatories in an 'ocean+1-D' model using the three conductance maps of resolution $3^\circ \times 3^\circ$, $1^\circ \times 1^\circ$ and $0.3^\circ \times 0.3^\circ$. Fig. 9 compares predicted C-responses for three resolutions for two representative observatories, HER and KNY (Kanoya, Japan), where ocean effect is prominent, and where one observes different types of this effect (see more details about two types of anomalous behaviour due to the ocean effect in the next section). This figure exemplifies the fact that, indeed, proper resolution of the conductance map is essential to accurately describe the ocean effect. For example, a lateral resolution of $3^\circ \times 3^\circ$ is not detailed enough to fully account for the effect at Kanoya observatory (*cf*. right-hand plot in Fig. 9). Visual comparison of the results for the

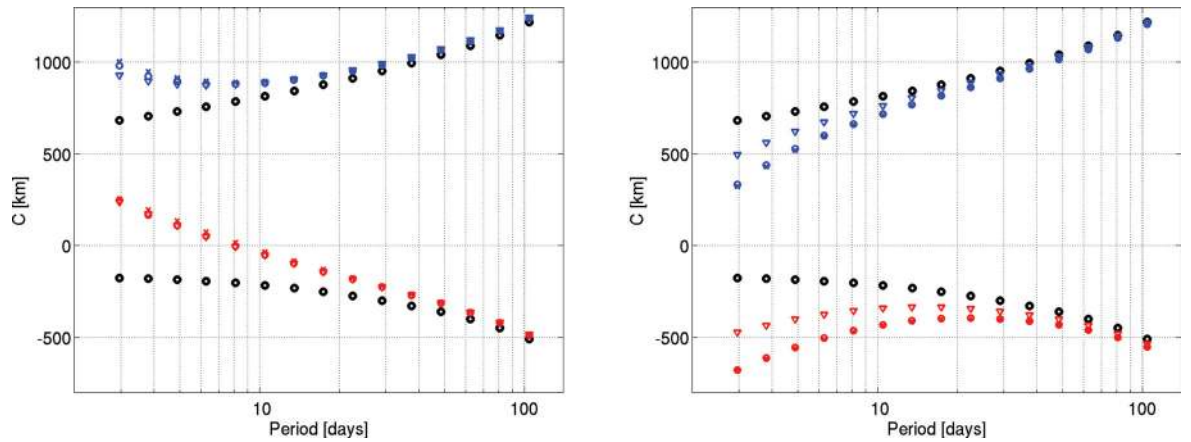

Figure 9. Ocean effect due to different ocean resolutions in the '1-D+ ocean' models. The left-hand plot presents the results for obseravtory HER (Hermanus), and the right-hand plot for observatory KNY (Kanoya; Japan). Coloured triangles, circles and crosses show the results for modelling with three conductance maps of resolution $3^\circ \times 3^\circ$, $1^\circ \times 1^\circ$, and $0.3^\circ \times 0.3^\circ$, respectively.

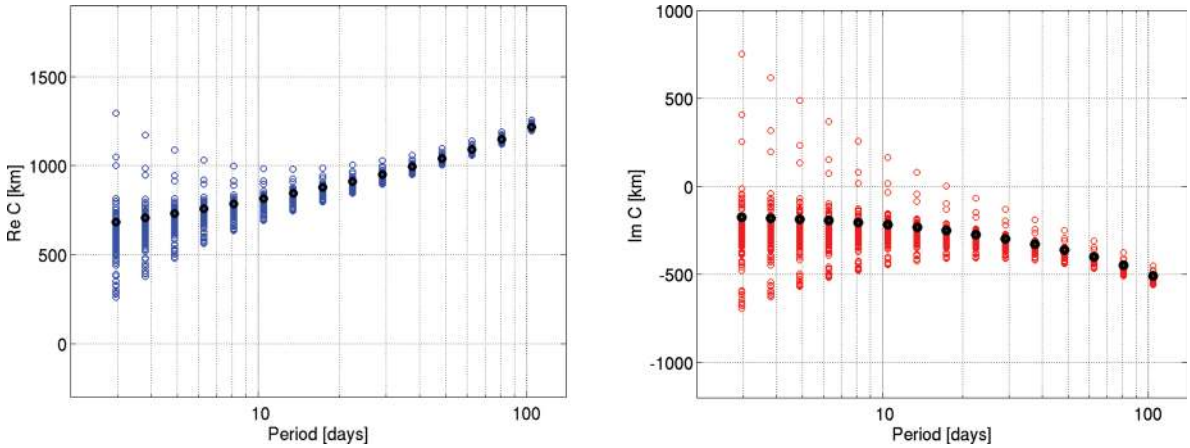

Figure 10. Variability of the responses due to the ocean effect. The left-hand plot shows real parts of the predicted *C*-responses, the right-hand plot shows the imaginary parts.

$1^\circ \times 1^\circ$ and the $0.3^\circ \times 0.3^\circ$ resolutions indicates that the $1^\circ \times 1^\circ$ grid is able to adequately model the ocean effect.

The variability of the responses for adopted $1^\circ \times 1^\circ$ resolution is shown in Fig. 10. We observe that the variability due to the ocean effect is substantial, especially at shorter periods, and that it can be traced to periods of 40 d. Variability of the imaginary part is, on average, 1.5 times larger than the variability seen in the real part. The maximum predicted variability at the shortest period are 1050 and 1500 km in real and imaginary parts, respectively. At a period of 40 d this variability drops to 100 and 300 km, respectively, although the imaginary part still exceeds the uncertainties of the responses. It is remarkable that the shape of the variability of the imaginary part of the predicted responses to a period of 20 d is in good agreement with the variability of the imaginary part of the experimental responses (*cf.* right-hand lower plot of Fig. 8). The agreement in the real part is worse (*cf.* left-hand lower plot of Fig. 8), where variability of the experimental responses is more or less constant throughout the whole period range and reaches 1600 km, which is substantially larger than the maximum variability of the predicted responses.

3.2 Two types of anomalous behaviour due to ocean effect

We discovered that two types of anomalous *C*-response behaviour can be seen due to the ocean effect. The first type is characterized by a substantial increase in both real and imaginary parts of the responses towards shorter periods (*cf*. left-hand plot in Fig. 9). Moreover at shorter periods the imaginary part at many coastal observatories becomes positive. Such a behaviour is not compatible with any 1-D conductivity structure, the responses of which always show up with a negative imaginary part (we adopted an $e^{i\omega t}$ time dependence convention to present the results), and a monotonically descending real part with decreasing period. Three end-member observatories, showing maximum ocean effect of this type, are KOU (Kourou, French Guiana), VSS (Vassouras, Brasil), and HER (Hermanus, South Africa).

The second type of anomalous behaviour is characterized by an excessive (compared to the 1-D case) decrease in both real and imaginary parts of the responses for decreasing period (*cf*. left-hand plot in Fig. 9). Three observatories that show the maximum ocean effect of this type are the Japanese observatories HTY (Hatizyo), KNY (Kanoya) and SSO (Simosato).

It is interesting that in some regions the relatively closely located observatories demonstrate the anomalous behaviour of different types of ocean effect. Fig. 11 illustrates this fact by showing the predicted responses at observatories Port Stanley (PST; South Atlantic) and Faraday island (AIA; Antarctica). The reason for this different behaviour in this particular region is that the observatories are situated at opposite sides of a strong electric current that flow between South America and Antarctica.

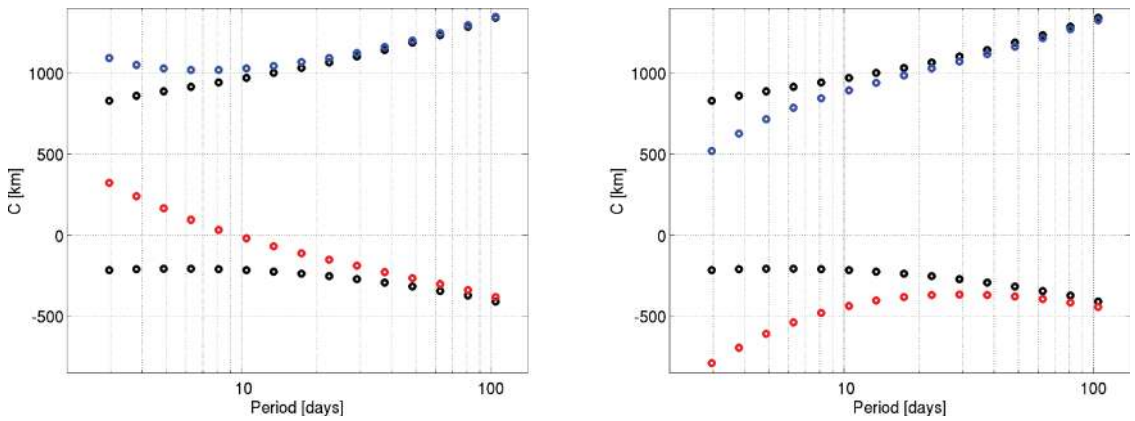

Figure 11. *C*-responses from the Port Stanley (PST) observatory in South America (left-hand plot) and from Faraday Island (AIA) observatory in Antarctic (right-hand plot) which are predicted in 'ocean + 1-D' model.

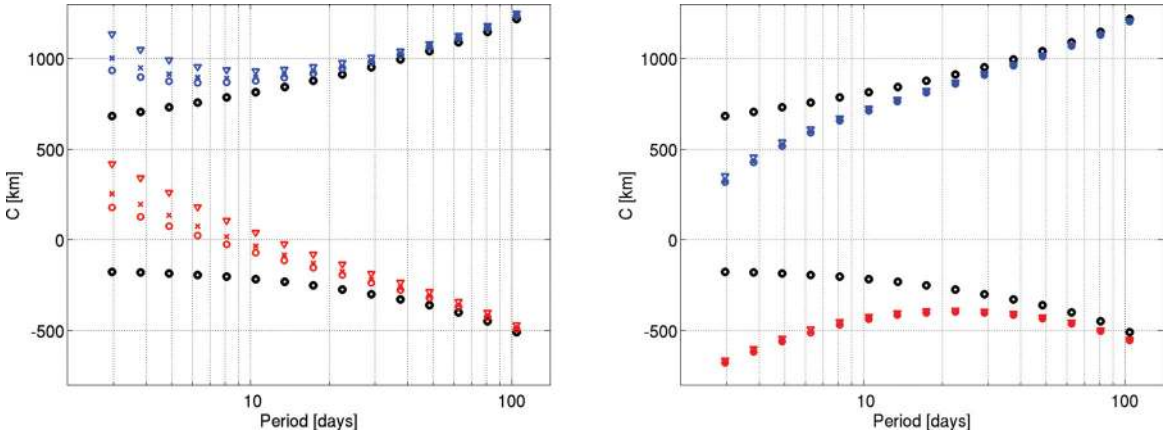

Figure 12. Dependence of the predicted responses at observatories Hermanus (left-hand plot) and Kanoya (right-hand plot) on lithosphere resistivity. Coloured circles, crosses, triangles are the responses for the 'ocean + 1-D' model with 300 Ohm-m, 3000 Ohm-m and 30000 Ohm-m lithosphere, respectively.

3.3 Dependence of the responses on 1-D conductivity structure beneath oceans

Next we studied to what extent the responses depend on the resistivity of the lithosphere. We calculated the responses in three 'ocean + 1-D' models using different values for lithospheric resistivity–300 Ohm-m, 3000 Ohm-m and 30000 Ohm-m, and fixing the model below to 1-D obtained by Kuvshinov & Olsen (2006). Fig. 12 compares predicted C-responses for observatories HER and KNY. This figure shows that for coastal observatories, like Hermanus, responses indeed depend on lithospheric resistivity.

Finally, we investigated how the results change if we vary the underlying 1-D section. For this purpose we take as a global 1-D section the local conductivity model derived by Khan *et al.* (2011) from the analysis of the responses estimated at Hermanus observatory. Note that Khan *et al.* (2011) achieved excellent agreement between very anomalous observed and predicted (in the model with oceans) responses at this observatory (see their fig. 4) by applying iteratively the correction scheme described by eq. (20). As for the case when we varied lithospheric resistivity, the responses for coastal observatories vary substantially if we change the underlying 1-D section. Fig. 13 illustrates this for the responses at Hermanus observatory.

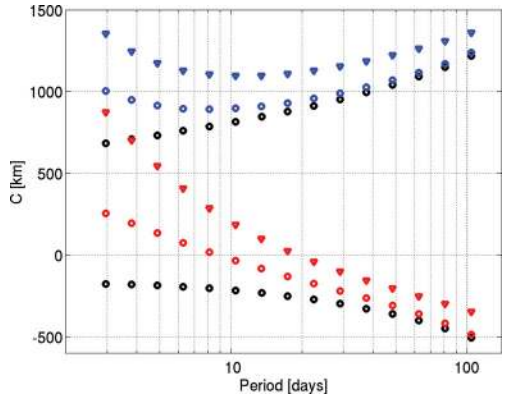

Figure 13. Dependence of the predicted responses at Hermanus observatory on 1-D conductivity profile. Coloured circles are the responses for the 'ocean + 1-D' model with 1-D conductivity profile from Kuvshinov & Olsen (2006), and triangles are the responses for the 'ocean + 1-D' model with 1-D conductivity profile recovered by Khan *et al.* (2011) from the Hermanus observatory data.

3.4 Correction for the ocean effect

The model studies in this section demonstrate that we must account for the ocean effect as accurately as possible in order to avoid interpreting this effect as arising from deeper structures. The best strategy to account for the distortions associated with a non-uniform distribution of the oceans and continents would be to include an oceanic layer of known conductance (with a lateral resolution of $1^\circ \times 1^\circ$) in the 3-D conductivity model, the deeper part of which we aim to image when inverting the data. However, only a coarser grid with a lateral resolution of $3^\circ \times 3^\circ$ is presently computationally feasible when performing our global 3-D inversion. Note that in our present version of the inverse solution all non-uniform layers have the same lateral resolution.

Alternatively, observed responses can be corrected for the ocean effect using eq. (20) where the predicted results in the model with oceans are calculated on a $1^\circ \times 1^\circ$ grid. This correction was employed by Kelbert *et al.* (2009) to isolate the influence of the oceans during their global 3-D inversion. However, our modelling studies have shown that the amount of correction (at least at very coastal observatories) depends strongly on the 1-D profile used during forward modelings. In order to apply corrections as consistently as possible we consider a more sophisticated correction scheme, which is described below.

We took the 1-D regional conductivity profiles recovered by Khan *et al.* (2011) for the six observatories distributed across the globe [Europe (FUR), South Africa (HER), China (LZH), Australia (ASP), North America (TUC) and North Pacific (HON)]. The localities are representative of a number of different tectonic settings, covering regions of continental extension (TUC), ocean (HON), relatively young continents (FUR and HER) and the stable archaean Australian craton (ASP). Fig. 15 shows these regional 1-D profiles for readers' convenience. Next we subdivided the selected (119) observatories into six clusters [EU (Europe), SA (South Africa), CN (China), AU (Australia), NA (North America), NP (North Pacific)] depending on distance to these six (reference) observatories. Finally, for each cluster of observatories we corrected the responses using eq. (20) but exploiting as a 1-D model the regional 1-D profile for the corresponding reference observatory. The last column of Table 1 provides information in which cluster the station belongs. Fig. 14 illustrates the result exemplified with observatories Hermanus and Kakioka.

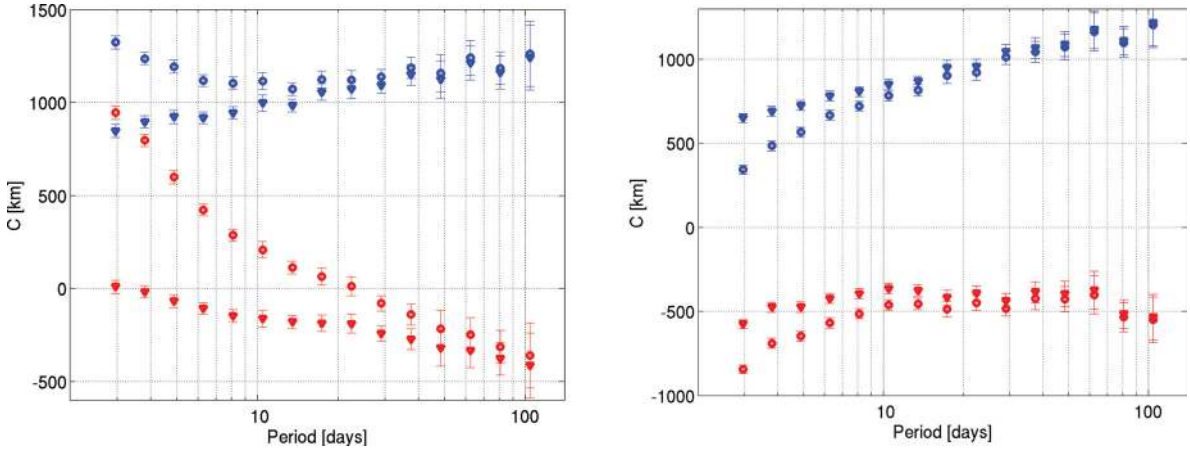

Figure 14. Results of the ocean correction for the Hermanus (left-hand plot) and Kakioka (right-hand plot) observatories. Circles with error bars show original experimental responses, triangles depict the responses corrected for the ocean effect.

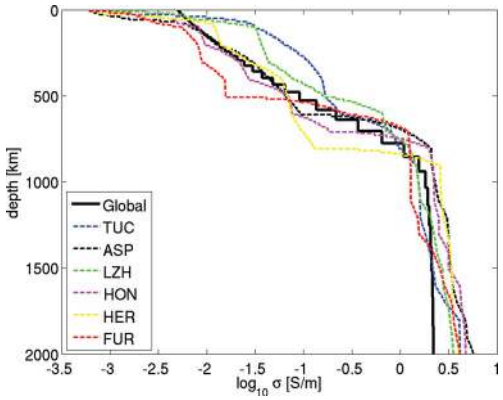

Figure 15. 1-D regional conductivity profiles recovered by Khan *et al.* (2011) for the six observatories distributed across the globe [Europe (FUR), South Africa (HER), China (LZH), Australia (ASP), North America (TUC) and North Pacific (HON)] which are used in this paper to correct the responses for ocean effect (see details in the text). Black curve shows global conductivity profile recovered by Kuvshinov & Olsen (2006).

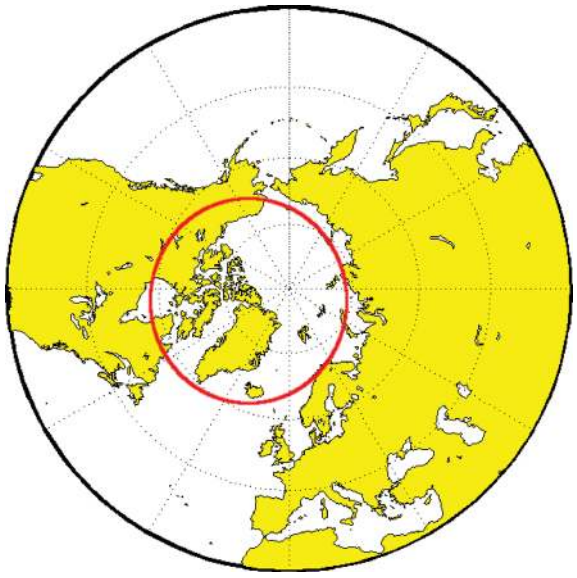

Figure 16. Adopted model of the auroral electrojet current system. This current system is represented by a circular infinitesimally thin line current flowing 23° apart from geomagnetic pole, at an altitude of 100 km.

4 AURORAL EFFECT IN THE RESPONSES

Another source of the variability of the experimental responses comes from auroral currents (polar electrojet) flowing in the ionosphere at an altitude of 110 km. This current system can to a first approximation be represented by a circular, infinitesimally thin line current flowing 23° apart from the geomagnetic pole (see Fig. 16). Fujii & Schultz (2002) demonstrated that the influence of this current system (auroral effect) is seen in the responses down to geomagnetic latitudes of 40°. In this section we investigate in detail the morphology of the auroral effect and propose a scheme to correct the experimental responses for this effect.

To start with, Fig. 17 presents the experimental responses at periods of 3.7, 10.5, 22.5 and 37.4 d from all observatories as a function of GM latitude. Two features in the response behaviour are clearly visible.

First, the behaviour of the responses both in real and imaginary parts show abrupt changes around 58° latitude. Note that in Section 2.2.3 we—based on the analysis of the squared coherency (*cf.* Fig. 5)—provided the reasons why we exclude the responses from the observatories higher than 58° latitude from the final data set. In this section we present the responses from those observatories just to demonstrate again that these data cannot be used for the interpretation.

Secondly, one can see that in the latitudinal band between 40° and 58° the real part of the responses clearly decays towards higher latitudes. Note that this behaviour of the real part is observed for all considered periods. In contrast, the imaginary part of the responses does not reveal a dependency on geomagnetic latitude in this band. Below we argue that this can be explained by the fact that there is weak induction effect from the auroral current system in the considered period range.

Fig. 18 shows a typical manifestation of the auroral effect in the responses at observatories located in the discussed latitudinal range, for example, the experimental responses at observatory Brorfelde (BFO; Denmark; $\vartheta = 55°$N GM), and at observatory Ekaterinburg (SVD; Russia; $\vartheta = 49°$N GM). For comparison black circles depict the predicted responses from the global 1-D conductivity profile derived by Kuvshinov & Olsen (2006). The auroral effect is seen as a strong decrease of the real part of the responses towards shorter periods. We also note that the imaginary part of the responses is

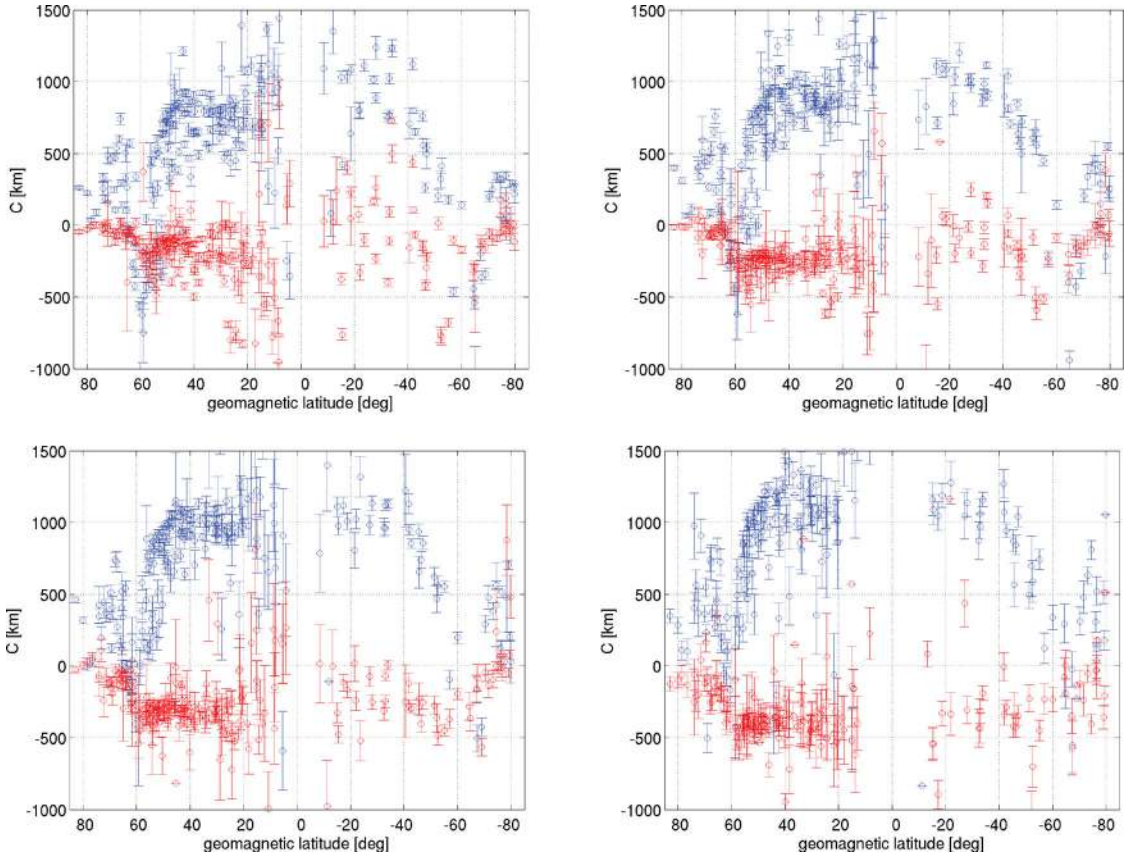

Figure 17. Real (blue) and imaginary (red) parts of the *C*-responses estimated for all observatories at periods of 3.7 d (upper left-hand plot), 10.5 d (upper right-hand plot), 22.5 d (lower left-hand plot) and 37.4 d (lower right-hand plot). The responses are shown as a function of GM latitude.

weakly influenced by the auroral electrojet as there is a small amount of induction occurring from this source. Moreover, the squared coherency for these observatories is substantially smaller than those obtained at lower latitude observatories (*cf.* Fig. 3).

To confirm this conclusion quantitatively we calculated magnetic fields at the Earth's surface induced by the auroral current, which has the geometry shown in Fig. 16. Fig. 19 presents the results for the Z and H components for a period of 22.5 d along the profile $\varphi = 30^\circ$ (in geomagnetic coordinates). Blue curves represent the external field, black and red curves show the results for the models with and without an ocean, respectively. One observes that the conducting earth (either with or without an ocean) only negligibly affects the external field.

4.1 Longitudinal dependence

Having found that the influence of the auroral current system can be traced in *C*-responses down to a geomagnetic latitude of 40° *globally*, we next discovered that the auroral effect in the responses reveals a strong longitudinal variability, at least in the Northern Hemisphere. Fig. 20 displays responses at two periods as a function of geomagnetic latitude for three regions: Europe, North

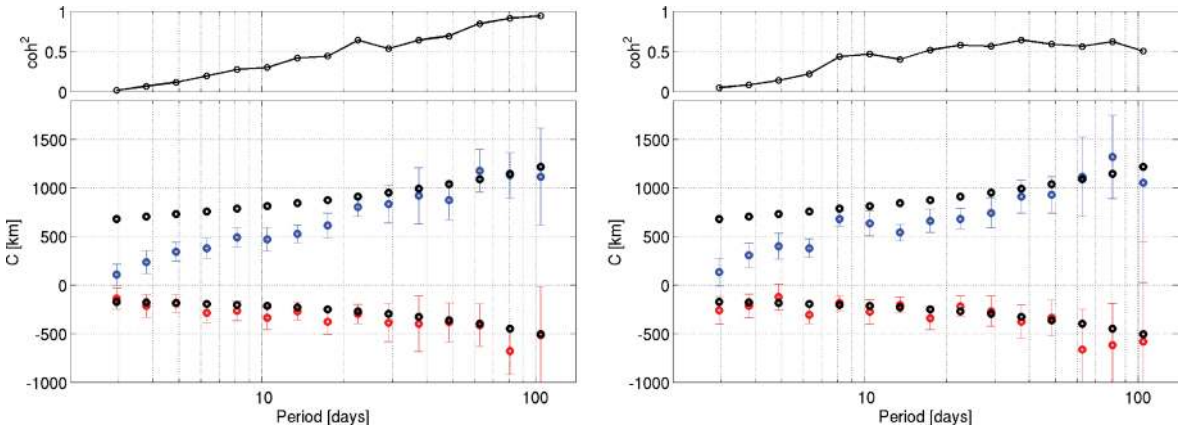

Figure 18. Experimental responses at two observatories located in geomagnetic latitude band between 40° and 58°. The left-hand plot shows the responses at Brorfelde (BFO; Denmark) observatory, the right-hand plot shows the responses at Ekaterinburg (SVD; Russia) observatory.

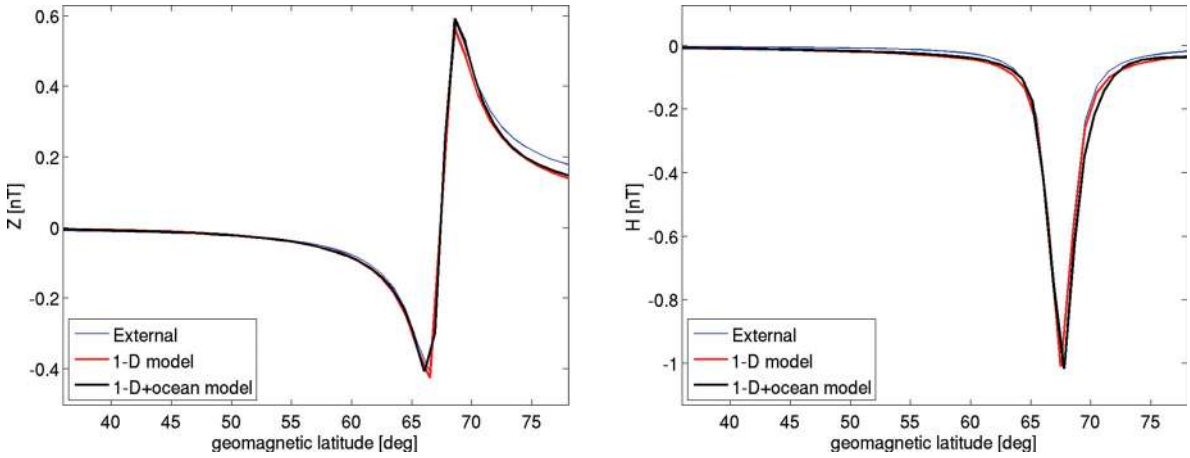

Figure 19. *Z* (left-hand plot) and *H* components (right-hand plot) of the real part of the magnetic fields at the Earth's surface excited by an auroral current. Blue curves depict external field, black and red curves show the results for the models with and without ocean, respectively. The results are for period of 22.5 d.

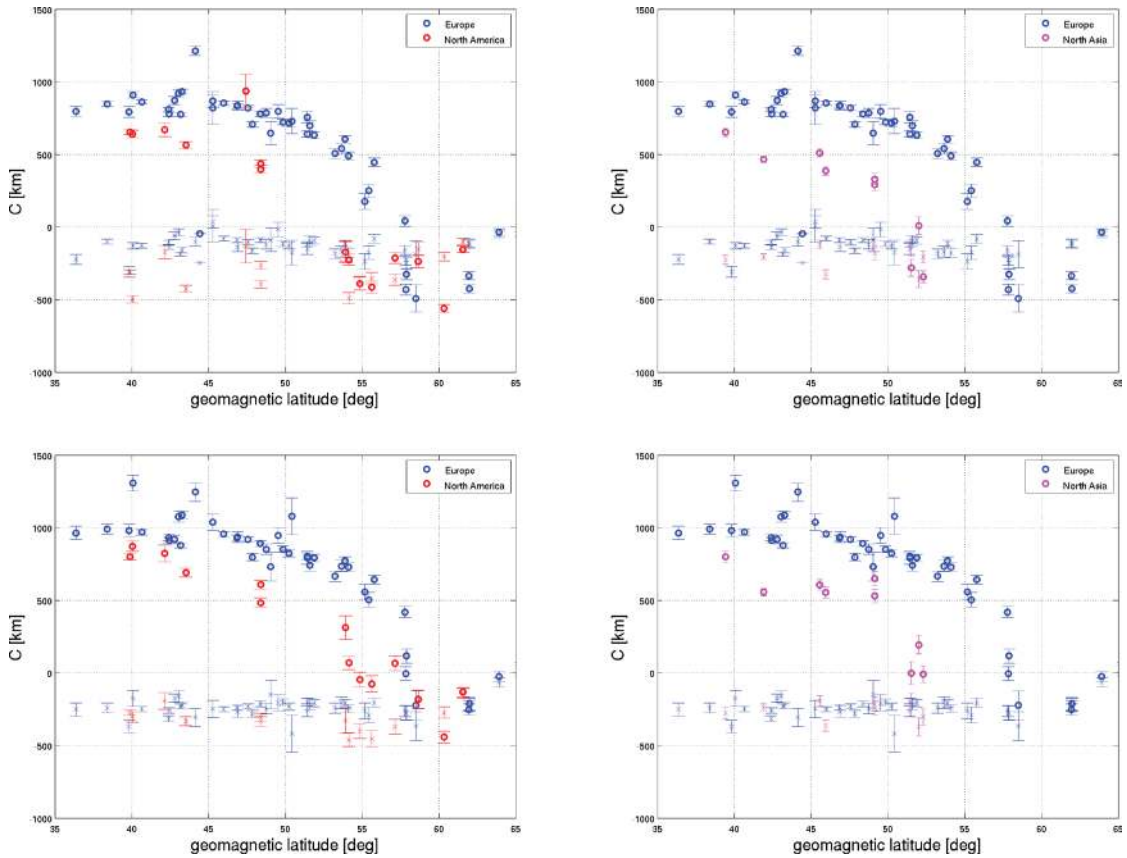

Figure 20. Comparison of the auroral effect in experimental *C*-responses in different regions. The left-hand plots show the comparison of the responses in Europe and North America, the right-hand plots show comparison of the responses in Europe and North Asia. Circles represent the real part of the *C*-responses, crosses—the imaginary part. Blue, magenta and red colours depict the results for Europe, northern Asia and North America, respectively. From the top to the bottom are the responses for periods 3.7 and 10.5 d.

America and northern Asia. It is clearly seen that the decay pattern of the real part of the responses towards the geomagnetic pole varies with region. Europe appears to be the region with the smallest level of distortion. (Note again that the imaginary parts are weakly affected by the auroral source in the latitudinal band between 40° and 58°). This suggests that the auroral electrojet has longitudinal variations either in strength or/and in spatial distribution. We have no conclusive explanation so far for what physical process is behind such variability of the auroral source. One can speculate (C. Finlay, personal communication, 2010) that the longitudinal variability of the auroral source can be governed by spatial inhomogeneity of the intensity of the main field which strongly deviates from dipolar structure in auroral regions and has pronounced patches exactly over North America and northern Asia (see Fig. 21). The enhanced field strength in these regions could perhaps help to explain this asymmetry in auroral ionospheric currents.

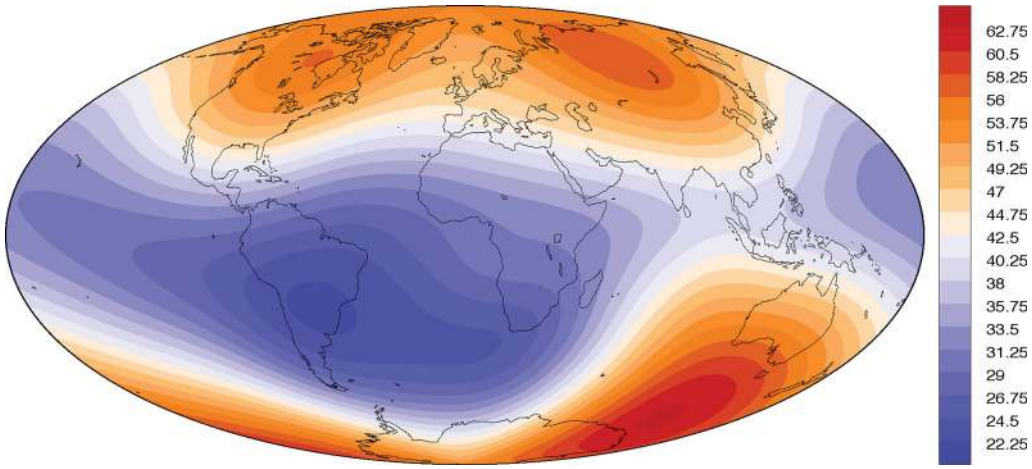

Figure 21. Intensity of the main magnetic field at 110 km altitude in 2010 from IGRF-11 model (Finlay *et al.* 2010).

4.2 Correction for the auroral effect

Given that the auroral signals appear independent of the Earth's conductivity, in addition to the longitudinal variability of the auroral effect, we have developed a scheme to correct the responses from observatories located between 40° and 58° latitude for this effect. We consider as before the model of the auroral current described in the beginning of Section 4. The correction scheme works as follows.

(1) Magnetic fields from the auroral current source, $Z_s^{\rm aur}(\omega)$ and $H_s^{\rm aur}(\omega)$, are calculated at the location of all considered observatories, with s denoting the specific observatory. During these calculations the choice of the conductivity model of the Earth is not relevant, since it does not influence the results as discussed earlier (*cf.* Fig. 19).

(2) Magnetic fields from a magnetospheric ring current source, $Z_s^R(\omega)$ and $H_s^R(\omega)$, are calculated for each of three regions, R. These regions are Europe (with geographic longitude from 330° to 45°), northern Asia (with geographic longitude from 45° to 180°) and North America (with geographic longitude from 180° to 330°). For these regions we used three different 1-D conductivity profiles derived by inversion of C-responses from the observatories of these regions, for which data are assumed not to be influenced by the auroral effect. For North America, Europe and northern Asia these observatories were Tucson (TUC; $\vartheta = 40°$N GM), Panagyurishte (PAG; $\vartheta = 40°$N GM) and Manzhouli (MZL; $\vartheta = 39°$N GM), respectively. Note that these 1-D models are compatible with those used for oceanic correction.

(3) We introduce complex-valued coefficients, $k_R(\omega)$, which we assume are specific for each region, R, and frequency, ω, and estimate the size of the auroral effect in this region by minimizing (with respect to k_R) the following functional

$$\sum_{s\in R}\left|\frac{C_s^{\rm mod}(\omega)-C_s^{\rm exp}(\omega)}{\delta C_s^{\rm exp}(\omega)}\right|^2 \stackrel{k_R(\omega)}{\longrightarrow} \min, \qquad (21)$$

where

$$C_s^{\rm mod}(\omega) = -\frac{a\tan\vartheta_s}{2}\,\frac{Z_s^R(\omega)+k_R(\omega)Z_s^{\rm aur}(\omega)}{H_s^R(\omega)+k_R(\omega)H_s^{\rm aur}(\omega)}. \qquad (22)$$

Fig. 22 demonstrates the results of fitting experimental responses using eq. (22) at a period of 10.5 d in Europe, North America and North Asia, respectively. Circles with error bars show the experimental responses, $C_s^{\rm exp}$, whereas crosses depict modelled responses, $C_s^{\rm mod}$. Fig. 23 shows the recovered coefficients k_g as a function of period. It is seen that these coefficients indeed vary from region to region, showing the largest differences in North America with the most decay occurring over longer periods.

(4) Finally, we correct the real parts of the experimental responses, for each region R and frequency ω as

$$\Re\{C_s^{\rm exp,corr}(\omega)\} = \Re\{C_s^{\rm exp}(\omega)\} + \Re\{C_{1D}^R(\omega)\} - \Re\{C_s^{\rm mod}(\omega)\}. \qquad (23)$$

Fig. 24 illustrates the application of this scheme for European observatories at a period of 13.5 d. Fig. 25 shows the results of the correction on the observatory Niemegk (NGK; $\vartheta = 51°$N GM; Germany) at all periods. One can see that the correction made the responses more compatible with the responses at lower latitude (*cf.* Fig. 3).

We applied this scheme only for the observatories located in the Northern Hemisphere. In the Southern Hemisphere no definitive conclusion could be made about the longitudinal variability of the auroral effect due to the lack of observatories in this region. Moreover, the responses from the very few Southern Hemisphere observatories located between 40° and 58° latitudes are also influenced by the ocean effect (fortunately, this is not the case for most of the observatories in this latitude band in the Northern Hemisphere), complicating the analysis. The latter fact is illustrated in Fig. 26, which demonstrates experimental responses at Faraday Island (AIA; $\vartheta = -55°$S GM; Antarctic) observatory. Here, a very strong decay in the real part of the responses at shorter periods is most probably due to cumulative effect of both—auroral electrojet and ocean. The imaginary part is also affected, but because of the ocean effect.

Our scheme of auroral effect correction is based on purely phenomenological approach and cannot be considered fully satisfactory. Indeed, one can argue that one-complex-valued parameter model is valid when magnetospheric ring current and auroral currents are coherent with each other, which is definitely not the case. However, we observe that our correction scheme makes the real parts of the responses at higher latitudes more consistent with the responses at lower latitudes.

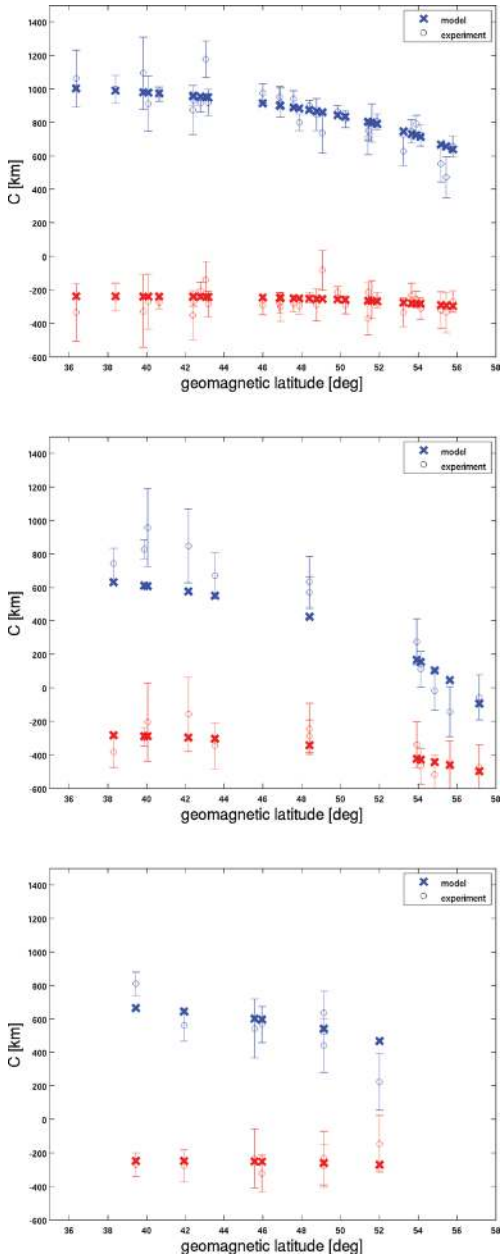

Figure 22. The results of fitting of experimental responses, $C_s^{\rm exp}$, and modelled responses $C_s^{\rm mod}$ for Europe (upper plot), North America (middle plot) and northern Asia (lower plot). Circles with error bars show the experimental responses, $C_s^{\rm exp}$, whereas crosses depict modelled responses, $C_s^{\rm mod}$. The results are for the period of 10.5 d.

5 3-D INVERSION OF THE EXPERIMENTAL RESPONSES

5.1 Detecting lateral variations in mantle conductivity

We formulate the inverse problem of conductivity recovery as an optimization problem such that

$$\phi(\mathbf{m}, \lambda) \underset{\mathbf{m}}{\rightarrow} \min, \tag{24}$$

with the penalty function

$$\phi(\mathbf{m}, \lambda) = \phi_d(\mathbf{m}) + \lambda \phi_s(\mathbf{m}), \tag{25}$$

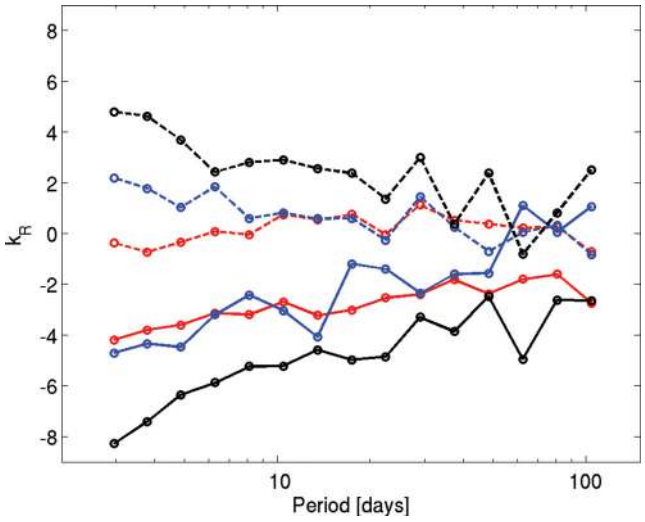

Figure 23. The recovered coefficients which were used to correct the observed C-responses for auroral effect. Red, blue and black curves depict the results for Europe, northern Asia and North America, respectively. Solid and dashed curves stand for real and imaginary parts of the coefficients, respectively.

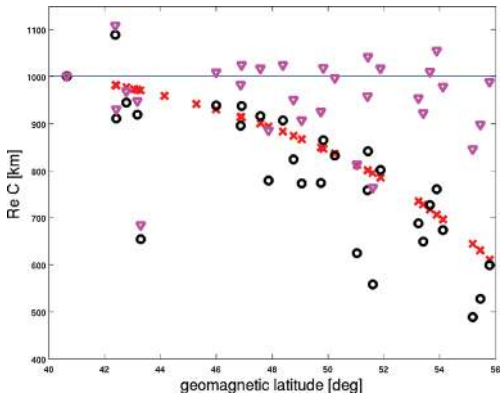

Figure 24. Results of the correction of the European responses for the auroral effect at period 13.5 d (see eq. 23). Blue line is the real part of the 1-D C-response, $\Re\{C_{1D}^R(\omega)\}$, on observatory PAG ($\vartheta = 40^\circ N$ GM), red crosses are the real parts of the modelled (see eq. 22) C-responses, $\Re\{C_s^{\rm mod}(\omega)\}$. Black circles are experimental values of the real parts of C-responses, $\Re\{C_s^{\rm exp}(\omega)\}$. Magenta triangles are the real parts of the corrected responses, $\Re\{C_s^{\rm exp,corr}(\omega)\}$.

where λ and $\phi_s(\mathbf{m})$ are a regularization parameter and a regularization term, respectively, and $\phi_d(\mathbf{m})$ is the data misfit

$$\phi_d(\mathbf{m}) = \sum_{\omega\in\Omega}\sum_{\mathbf{r}_a\in\text{Sites}} \left| \frac{C^{\rm mod}(\mathbf{r}_a, \omega, \mathbf{m}) - C^{\rm exp}(\mathbf{r}_a, \omega)}{\delta C^{\rm exp}(\mathbf{r}_a, \omega)} \right|^2. \tag{26}$$

Here $C^{\rm mod}(\mathbf{r}_a, \omega, \mathbf{m})$ and $C^{\rm exp}(\mathbf{r}_a, \omega)$ are the predicted and observed C-responses at observation site $\mathbf{r}_a$ and at frequency ω, and $\delta C^{\rm exp}(\mathbf{r}_a, \omega)$ is the uncertainties of the observed responses. 'Sites' define the locations of the geomagnetic observatories, 'Ω' define the frequencies under consideration. Vector $\mathbf{m}$ represents the model parameters that describe the 3-D conductivity distribution in the model. We work with a regularization term of the form

$$\phi_s(\mathbf{m}) = \{W\mathbf{m}\}^T\{W\mathbf{m}\}, \tag{27}$$

where the superscript T means transpose and W presents a regularization matrix which—together with the regularization parameter

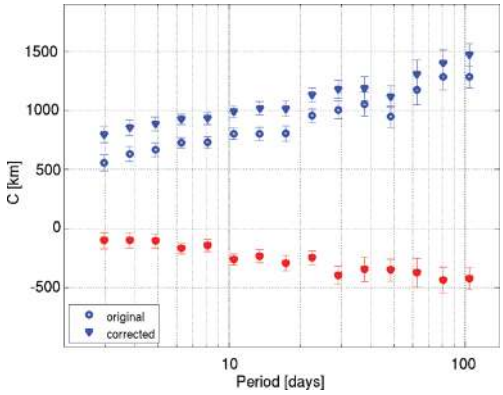

Figure 25. Results of the auroral correction for the Niemegk (NGK) observatory in Germany. Circles with error bars show original experimental responses, triangles—real part of responses corrected for the auroral effect.

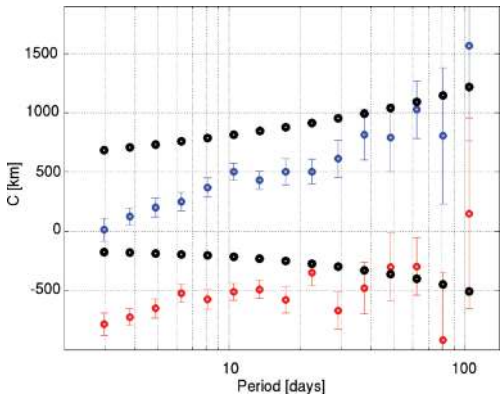

Figure 26. Experimental responses at Faraday Island (AIA) observatory.

λ—controls the model smoothness. As a smoothing matrix the finite difference approximation to the gradient operator is used which, in particular, means that horizontal and vertical smoothing is equal. The details of our 3-D inverse solution are explained in the companion paper by Kuvshinov & Semenov (2012).

For the 3-D inversion of our data set it was assumed that lateral heterogeneities are present in the depth range 410–1600 km. Our decision not to search conductivity variations outside 410–1600 km is based on the fact that we interpret the *C*-responses in the period range 2.9–104 d. This period range corresponds to the range of penetration depth of EM field from about 600 km to 1200 km, as the real part of the experimental responses in a 1-D environment–being proxy for penetration depth (Weidelt 1972)—tells us (see for example Fig. 3). Thus we assume that outside this depth range there is a little sensitivity of the data to conductivity variations. However, trying to be on the safe side we enlarged further the target depth range up to 410–1600 km. We performed trial inversions where we searched for conductivity variations in upper mantle (at depths smaller than 410 km), however, not to specify the conductivity variations at these depths (which we think one can hardly resolve using the data in the considered period range) but to understand whether our results will change in the target (410–1600 km) depth range. As expected we did not see substantial difference between the results (not shown in the paper) of inversions when expanded depth range is considered and the results of inversion when lateral heterogeneities are present in the depth range 410–1600 km.

We parametrized the 3-D conductivity distribution at these depths by five spherical inhomogeneous layers of 110, 150, 230, 300 and 400 km thickness. The thicknesses of the two upper layers were

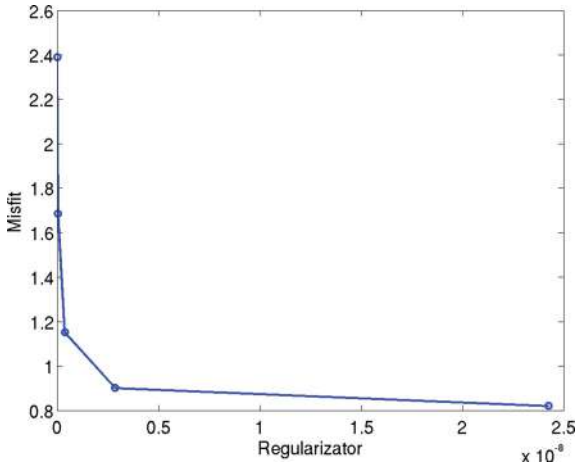

Figure 27. Typical shape of L-curve for our 3-D inversions. Regularization term is from eq. (27).

chosen in accordance with seismic studies which show compositional changes at depths 410, 520 and 670 km. The thicknesses of the three lower layers coincide with those used by Kelbert *et al.* (2009) to simplify the comparison with their results which will be discussed later in this section. The layers were embedded into an *a priori* 1-D section obtained by Kuvshinov & Olsen (2006). Introducing *a priori* means that we will consider as a vector of our model parameters

$$\mathbf{m} = \left(\ln\left(\frac{\sigma_1}{\sigma_1^0}\right), \ln\left(\frac{\sigma_2}{\sigma_2^0}\right), \ldots, \ln\left(\frac{\sigma_{N^{\rm inv}}}{\sigma_{N^{\rm inv}}^0}\right)\right), \tag{28}$$

where $\sigma_i^0,\ i = 1, 2, \ldots, N^{\rm inv}$ are the conductivities of the *a priori* section. This 1-D section remains unchanged during 3-D inversion. The choice of this 1-D model is motivated by the following reasoning. 1-D conductivity model by Kuvshinov & Olsen (2006) is based on analysis of satellite data which are characterized by better (compared with ground-based data) global coverage. This enables one to derive a globally-averaged 1-D conductivity profile which is not biased towards one or another region, especially if the ocean effect is corrected for, as it was done in that paper. Moreover this model is based on a *global* response, calculated from the ratio of external and internal coefficients representing the dominating term of spherical harmonic expansion of the magnetic potential. From our point of view the work with global responses is preferable if one aims to derive globally-averaged 1-D conductivity profile. We cannot claim that this 1-D model is the best-fitting model to the observatory *C*-responses but we see remarkable overall accord (both in real and imaginary parts) between the cloud of experimental observatory *C*-responses and theoretical responses from aforementioned 1-D section (*cf*. Fig. 8, where the theoretical responses are shown as black circles).

The model is excited by a source that is described by the first zonal harmonic in a geomagnetic coordinate frame. All forward problem calculations were performed on a $3^\circ \times 3^\circ$ grid. The lateral resolution of the inverse domain was chosen to be $9^\circ \times 9^\circ$. For each inversion run the regularization parameter was determined using the L-curve criterion (*cf.* Hansen 1992). Fig. 27 presents a typical L-curve for one of our 3-D inversions; for all runs the regularization parameter was taken to be in the vicinity of the knee of the L-curve. Note that hereinafter the misfit stands for the normalized misfit

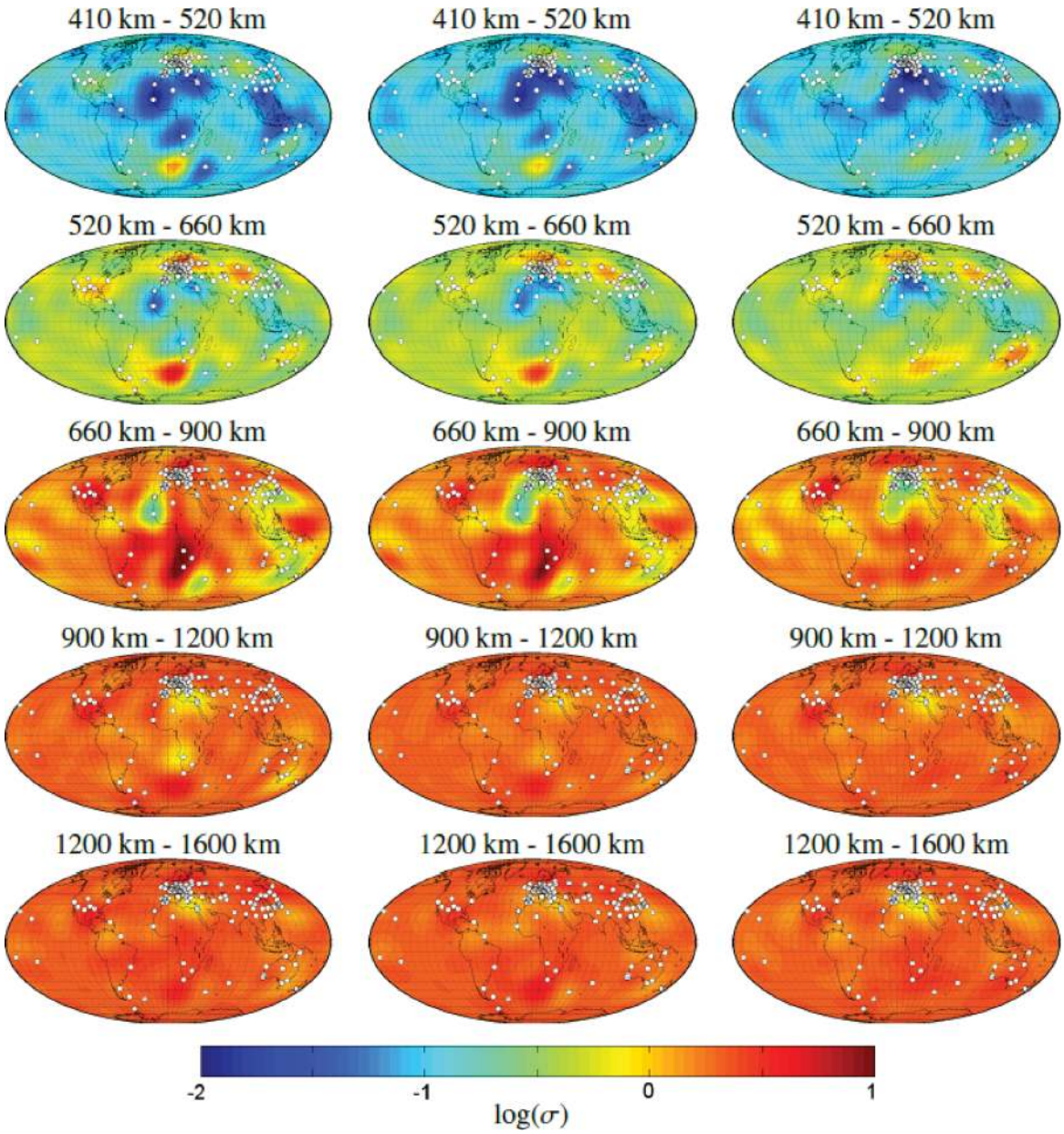

Figure 28. Results of our 3-D inversion. The left-hand column of plots presents the results of inversion of uncorrected responses. Middle column—the results of inversion of the responses corrected for the auroral effect. Right-hand column—the results of inversion of the responses corrected for the auroral and the ocean effects.

defined as

$$\phi_d^N = \frac{1}{N_{\text{data}}} \sum_{i=1}^{N_{\text{obs}}} \sum_{j=1}^{N_T(i)} \left| \frac{C_{ij}^{\text{pred}} - C_{ij}^{\text{exp}}}{\delta C_{ij}} \right|^2 . \tag{29}$$

Here $N_{\text{data}} = \sum_{i=1}^{N_{\text{obs}}} N_T(i)$, and C_{ij}^{exp}, C_{ij}^{pred} and δC_{ij} are experimental responses, predicted responses and uncertainties of experimental responses, respectively, of the ith observatory at the jth period. The expression for N_{data} means that for some observatories the number of analysed periods is less than 15.

To detect robust features in the conductivity images we performed three 3-D inversion runs, which differ by an amount of the corrections applied to the data. We did not present a discussion on the resolution of the conductivity obtained by 3-D inversion using our set of observatories and our period range since we find that the resolution analysis performed by Kelbert *et al.* (2009) already does this job using similar set of observatories and periods. In the first run, data were neither corrected for ocean nor for auroral effects. The ocean was included in the model as an additional thin (surface) inhomogeneous layer with a prescribed and fixed (during the inversion) conductance with a lateral resolution of $3^\circ \times 3^\circ$. Results from this 3-D inversion (global conductivity distributions in five inhomogeneous layers) are presented in the left-hand column of Fig. 28. Note that we present in this figure not the raw results—which are piecewise constant conductivity distributions—but their smoothed version. The smoothing procedure is based on a spherical harmonic filtering of the raw results up to spherical harmonics of degree 9. We present the filtered results only when we discuss the global images. This is motivated by the fact that we aim to compare these images

with the global results of Kelbert *et al.* (2009), who used a spherical harmonic parametrization (up to degree 9) of their inverse domain, as well as with the global filtered results of Tarits & Mandea (2010). Note also that here our results are shown as decimal logarithms of conductivities. To be able to compare the results at different depths the same scale is employed for all five layers. A scale range between −2 and 1 corresponds to a range in conductivity between 0.01 S m^{-1} and 10 S m^{-1}. It is also important to emphasize at this stage that one must interpret the results of inversion in many regions (e.g. in equatorial and oceanic regions) with extreme care—lack of observation precludes any conclusive inferences about conductivity distributions in these regions. For example, the decrease in conductivity beneath Indonesia in the first three layers is not supported by data.

In the second run we also included the oceanic layer in the model but corrected the data for the auroral effect (see Section 4 for details of the correction scheme). The recovered conductivities are shown in the middle column of Fig. 28. Unfortunately our sophisticated scheme of data correction for the auroral effect only partly improves the results of the inversion (normalized misfit appeared to be slightly less). We nonetheless observe enhanced conductivity in our images in Northern Europe (at least in the first three layers) which is—we believe—an artefact dictated to a large extent by an inappropriate correction for the auroral effect. Discernible differences are seen only beneath North America (in the two first layers) where an implementation of the correction led to a less pronounced conductivity anomaly.

Finally, in the third run we inverted data corrected both for ocean and auroral effects. Our correction scheme for the ocean effect is outlined in Section 3. We exclude the surface layer from the model, assuming that our correction scheme suppresses the effect of the ocean in the responses. Note that to justify the correction scheme we successfully verified that the results from inversion of original responses when surface oceanic layer (of $3^\circ \times 3^\circ$ resolution) is included in the model are similar to the results from inversion of corrected responses (using $3^\circ \times 3^\circ$ resolution predictions to correct for the ocean effect) when surface oceanic layer is not included in the model. The results of the third inversion run are shown in the right-hand column of Fig. 28. Here we observe substantial changes in the conductivity distribution in the first three layers beneath two regions: South Africa and Australia. The spurious anomaly to the south of the African continent that was seen in the results of the two first runs is much decreased in amplitude. The results of this run will be compared with results from other semi-global and global 3-D studies.

A closer look at the results presented in Fig. 28 reveal the following common features: (1) at depths between 410 and 900 km lateral variations in conductivity are rather prominent, reaching 1.5 orders of magnitude, and below 900 km the conductivity variations diminish with depth; (2) all inversions show a decrease in conductivity beneath southern Europe and northern Africa at all considered depths, and this feature will be discussed later in this section; (3) an increase of conductivity is discernable beneath China at depths between 520 and 900 km. This is in agreement with the results of Ichiki *et al.* (2001). We also see a prominent anomaly beneath northern Europe but we attribute this feature to an artefact associated with an underestimation of the auroral effect in the corrected responses. Alternatively, one could also speculate about the presence of an enhanced conductivity beneath Australia and South Africa. However, prior to scrutinizing the conductivity maps it is also important to emphasize that results for equatorial and oceanic regions have to be interpreted with extreme care given lack of observatory data from these regions, and since the amount and the shape of this anomalous behaviour strongly varies with inversion settings.

Fig. 29 shows how well the results of the 3-D inversion (third run) fit the data. The figure presents the misfits at each observatory for a starting 1-D conductivity model (left-hand plot) and for the recovered 3-D model (right-hand plot). It is seen that for most of the observatories the 3-D inversion substantially decreases the misfit. This is especially true for European and Japanese observatories.

Fig. 30 shows the evolution of the overall misfit with respect to number of iterations performed. During inversion the misfit drops from 2.4 to 0.98, and after 20 iterations the solution has converged with almost no improvement of misfit. For comparison, the first two inversion runs achieved misfits of 1.7 and 1.6, respectively.

In conclusion of this section it is worthwhile to mention that we performed a set of additional inversions to explore whether our results are robust enough with respect to initial guess on the model. It is remarkable that by starting with different (but plausible) 1-D models we observed similar resulting conductivity distributions (not shown in the paper).

5.2 Comparison with semi-global 3-D studies

Koyama (2001) was the first to develop and apply a rigorous 3-D inversion scheme to interpret ground-based *C*-responses on a semi-global scale. In later studies (Fukao *et al.* 2004; Koyama *et al.* 2006; Utada *et al.* 2009; Shimizu *et al.* 2010b) his inverse solution was exploited to analyse EM data, mostly beneath the northern Pacific region. The authors investigated voltage data from trans-Pacific submarine cables and magnetic field data from circum-Pacific geomagnetic observatories. We note that Utada *et al.* (2009) also analysed data from Europe (to be discussed later in this section). In the above studies lateral heterogeneity was assumed to exist between 350 and

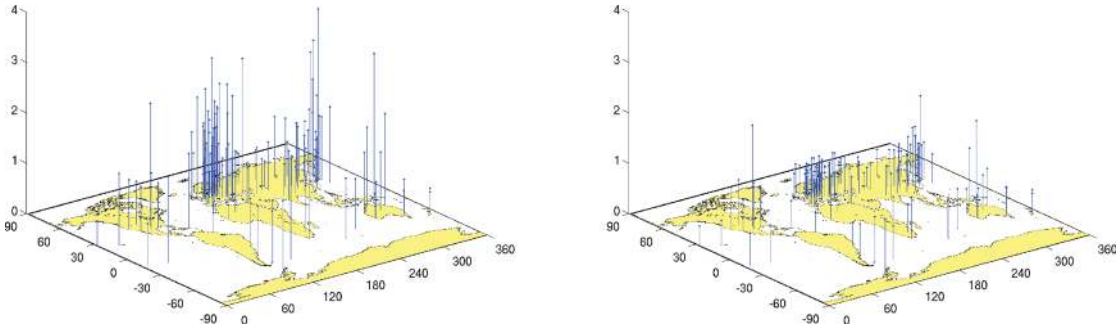

Figure 29. Starting misfit (left-hand plot) versus final misfit (right-hand plot).

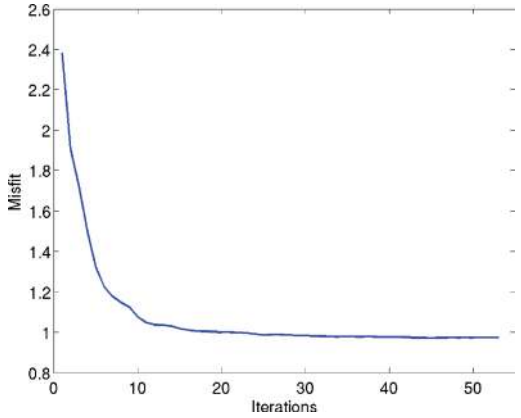

Figure 30. Misfit evolution during the 3-D inversion.

850 km depth, thus aiming to resolve the electrical conductivity structures in and around the transition zone (TZ).

We compare our results with the most recent results obtained by Shimizu *et al.* (2010b). Shimizu *et al.* (2010b) inverted GDS responses at nine periods between 5 and 35 d from 13 observatories, and MT responses at nine periods between 1.7 to 10.5 from eight trans-Pacific cables. The 1-D conductivity model beneath the North Pacific obtained by Shimizu *et al.* (2010a) was employed as an *a priori* model in this inversion. The grid spacing for the forward problem was $2^\circ \times 2^\circ$ laterally and 50 km radially. The size of each block in the final inversion domain was $10^\circ \times 10^\circ$ laterally and 100 km radially, comprising a total of $N = 19 \times 9 \times 5$ unknowns. Absolute values of the Laplacian of $\mathbf{m} - \mathbf{m}_0$ represented the regularization term in horizontal directions. No regularization of the model parameters in the vertical direction was applied. The right-hand plots of Fig. 31 show the resulting 3-D conductivity model. The authors detected three features in the TZ: (1) a high-conductivity anomaly beneath the Philippine Sea; (2) a high-conductivity anomaly beneath the Hawaiian Islands, and (3) a low-conductivity anomaly beneath and in the vicinity of northern Japan.

Left-hand plots in the same figure show our results for the same region and for similar depths. We plot $\log_{10}(\frac{\sigma_{3D}}{\sigma_{1D}})$, where σ_{3D} is our resulting conductivity and σ_{1D} is the 1-D *a priori* conductivity profile of Kuvshinov & Olsen (2006). Note that since the authors of these semi-global studies presented the piecewise constant conductivity distributions we apply the same strategy, showing in this section the raw (blocky) 3-D results. It looks as though our model somewhat over-determined, despite the model was selected based on *L*-curve technique which seems does not work satisfactorily in the regions with poor coverage by the data, such as the North Pacific region. The most prominent difference between our results and theirs is seen in the region beneath the Hawaiian islands, where our inversion shows more resistive structures instead of the more conductive structures recovered by Shimizu *et al.* (2010b). It should be noted that their results in this region are probably more conclusive than ours due to the fact that they used additional ('cable') data in these regions. As for regions beneath Japan and China our results seem to be closer to the results of the global 3-D model by Kelbert *et al.* (2009), which we will discuss in the next section. Note also that Shimizu (2010b) did not use the data from observatories in northern China, and thus their observatory distribution was not able to resolve the conductivity anomalies beneath this region.

Utada *et al.* (2009) constructed a 3-D conductivity model beneath Europe in depth range between 400 and 800 km. They inverted *C*-responses obtained in the period range between 5 and 50 d from 12 European observatories. As an *a priori* model they used the 1-D model for the northern Pacific region (Utada *et al.* 2003). The grid spacing for the forward problem calculations was $1^\circ \times 1^\circ$ laterally and 50 km radially. The size of each block in the inversion domain was $5^\circ \times 5^\circ$ laterally and 100 km radially, resulting in a total of $N = 9 \times 9 \times 5$ unknowns. No regularization was applied during inversion. The authors were interested in the conductivity distribution in the TZ, at depths between 400 and 700 km. The right-hand side of Fig. 32 shows their conductivity anomaly maps as well as the results of global *P*- and *S*-wave tomography studies (Megnin & Romanowicz 2000; Obayashi *et al.* 2006), with $\delta V_{P(S)}$ defined as

$$\delta V_{P(S)} = \frac{V_{P(S)}^{\mathrm{mod}} - V_{P(S)}^{\mathrm{PREM}}}{V_{P(S)}^{\mathrm{PREM}}} \cdot 100 \text{ per cent}, \tag{30}$$

where $V_{P(S)}^{\mathrm{mod}}$ are the $P(S)$-wave velocities from the 3-D study, and $V_{P(S)}^{\mathrm{PREM}}$ are the $P(S)$-wave velocities from preliminary reference earth model (PREM; Dziewonski & Anderson 1981).

The authors found that the most notable feature in their results is the correlation between the low-conductivity and high-velocity anomalies beneath the central and southern parts of Europe, where slab material subducted from the Tyrrhenian trench stagnates in the TZ (Faccena *et al.* 2003). They claim that such a correlation implies that the low-conductivity and high-velocity characteristics of the stagnant slab (Fukao *et al.* 2001) have a common origin, most likely temperature, and thus that there is no need to assume an additional conduction mechanism (e.g. hydrogen conduction) to explain a particular conductivity anomaly. These results led the authors to the inference that the TZ beneath Europe is relatively dry. Our results (left-hand plots)—using a different data set and different modelling technique—confirm this conclusion, with low-conductivity regions beneath the central and southern parts of Europe. In the images from both studies we see enhancement of conductivity in the northern and northwestern parts of Europe, but we believe that this may be an artefact related to the auroral effect, which is still present in the corrected experimental data.

5.3 Comparison with global 3-D studies

Kelbert *et al.* (2009) obtained the first global 3-D model of mantle electrical conductivity. They parametrized the 3-D conductivity distribution at depths between the surface and 1600 km by eight spherical inhomogeneous layers of 100, 150, 160, 110, 150, 230, 300 and 400 km thickness, in each of which lateral conductivity variations around the 1-D reference model of Kuvshinov & Olsen (2006) are parametrized by spherical harmonics up to degree and order 9. Conductivity jumps at 410, 520 and 670 km were allowed in order to mimic major mineral phase transitions in mantle. Below 1600 km the layers were assumed to be homogeneous with a fixed conductivity value. They used a compilation of the *C*-responses at 59 observatories from the studies of Fujii & Schultz (2002, responses from 53 observatories) and Schultz & Larsen (1987, responses from 6 observatories). The responses were estimated at 28 periods from 5 to 106.7 d. The lateral grid for forward problem calculations was chosen as $10^\circ \times 10^\circ$. To account for the ocean effect eq. (20) was applied, where the predicted responses were calculated with the use of integral equation (IE) solver of Kuvshinov (2008) using a much denser grid ($1^\circ \times 1^\circ$) to represent non-uniform oceans. The right-hand plots in Fig. 33 show the results of Kelbert *et al.* (2009). The authors note that in regions with poor data coverage, including most of Africa, South America and the Indian and South Pacific Oceans,

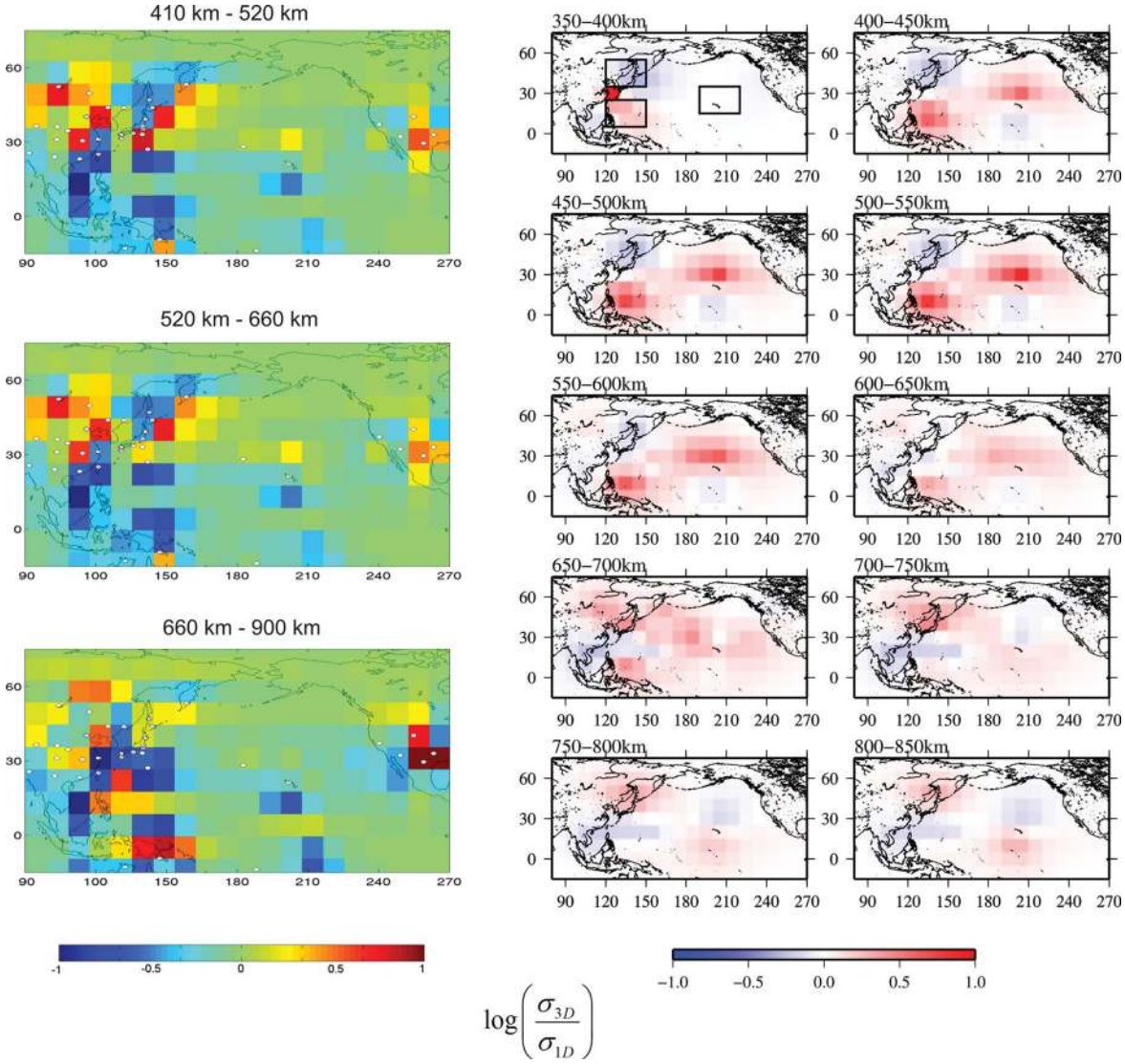

Figure 31. Comparison of our results (left-hand column of plots) with results from Shimizu *et al.* (2010b) study (two right-hand columns of plots).

conductivity is poorly constrained at all depths. Their inversion suggests enhanced conductivity at TZ depths along the circum-Pacific margin extending from western North America, through the Aleutian arc and eastern Asia, and into the Indian Ocean and Australia. Most notably, higher conductivities are found beneath Japan, eastern China, and in the areas of the Izu-Bonin and Tonga slabs. The central Pacific basin is seen to be more than an order of magnitude more resistive than the surrounding conductive regions. The left-hand plots in Fig. 33 show our results for comparison. The images differ in detail (for example, they differ beneath North America), but nonetheless reveal two common features: (1) reduced conductivity beneath southern Europe and northern Africa, and (2) enhanced conductivity beneath Japan and eastern China. The former is in agreement with the results of the semi-global study of Utada *et al.* (2009), while the latter, an enhanced conductivity beneath eastern China, is in accord with the results of Ichiki *et al.* (2001). However, high conductivities beneath Japan and low conductivities beneath Hawaii contrast with the results of Shimizu *et al.* (2010b). In addition, both inversions show enhanced conductivities in polar regions. This is, as already remarked, likely an artefact due to inappropriate accounting/correction for the auroral source effect. Visible differences are also present in lower layers, where our results are more conductive and show less lateral variability.

Recently Tarits & Mandea (2010) developed a 3-D EM time-domain technique to invert 32 years (1958–1990) of magnetic monthly mean values from 120 geomagnetic observatories to image the conductivity in the middle mantle. Their interpretation scheme includes two steps. As a first step a source field model and an initial 1-D conductivity profile are determined. To find a source they used a potential representation of the magnetic field. The authors obtained time-series of external and internal coefficients up to degree $n = 3$ using a regularized least-squares method. A 1-D conductivity profile was then obtained by performing a regularized inversion of global C-responses. C-responses were estimated using time-series of external and internal coefficients from dominant term ($n = 1$, $m = 0$) of spherical harmonic expansion.

3-D inversion was initiated with a 1-D conductivity model obtained in an initial step. The parameters for the inversion are the

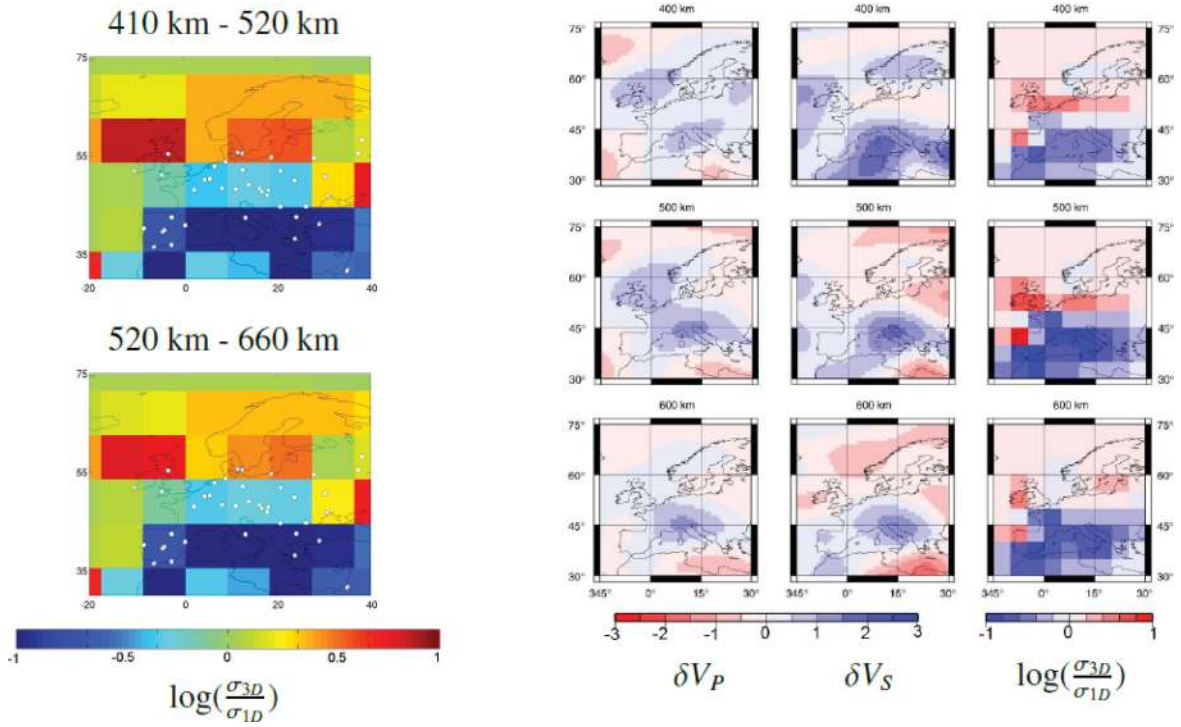

Figure 32. Comparison of our results (left column) with results from Utada *et al.* (2009) study.

conductivity in the cells of the inversion grid. Only the layer between 900 and 1400 km was assumed to be heterogeneous. Other layers were fixed to be homogeneous with conductivities fixed to their initial 1-D model. Tarits & Mandea (2010) used a grid with lateral resolution of $15^\circ \times 15^\circ$ (in both forward and inverse domains), thus estimating conductivity in $12 \times 24 = 288$ cells. The right-hand plots in Fig. 34 present their results filtered up to spherical harmonic degree 7. Our results for overlapping depth ranges are shown in the left-hand plots. The results of Tarits & Mandea (2010) reveal low conductivities beneath the Australian region, western Africa, near Japan and North and Central America, and high conductivities in eastern Africa and southeastern Asia. When compared with our results significant discrepancies can be observed. The most striking feature of the model by Tarits & Mandea (2010) is that it shows much stronger conductivity contrasts (up to 3 decimal logarithmic units) than our model (less than 1 log unit). It is interesting however that the reduced conductivity anomaly beneath southern Europe and northern Africa is recovered in both studies.

5.4 Comparison with global 3-D seismic studies

Lateral variation of electrical conductivity and seismic velocity are caused by compositional and temperature changes in the mantle with global geodynamics. Good (anti)correlation is expected when temperature variations are the leading process in a dry mantle (e.g. Shankland *et al.* 1993; Utada *et al.* 2009; Verhoeven *et al.* 2009): in regions with increasing temperature, the velocity decreases while the conductivity increases. This means that high conductivity corresponds to low velocity or vice versa.

There are several tomography models of the mid-mantle available (e.g. Becker & Boschi 2002; Romanowicz 2003). Della Mora *et al.* (2011) synthesized the common large-scale features, which are observed in *P*- and *S*-wave models, and created mean models, shown in two right-hand columns of plots in Fig. 35. In the middle column the resulting *P*-wave distributions of the *P*-mean model of Della Mora *et al.* (2011) in five layers are presented. The results are for depths between: 399 and 498 km, 498 and 598 km, 678 and 797 km, 997 and 1096 km and 1395 and 1495 km. The depths of these layers were chosen to correspond to the depths of our five inhomogeneous layers. In the right-hand column of Fig. 35 the *S*-wave distributions in the *S*-mean model of Della Mora *et al.* (2011) are shown for the same layers. $\delta V_{P(S)}$ is defined as in eq. (30). The left-hand column in Fig. 35 shows our 3-D results.

A very tentative comparison of our EM results with those from seismic studies shows that different trends are observed (at least in two shallower layers). In northern Africa, for example, low conductivity corresponds to high velocity. However, in Australia we see opposite trend: EM inversion reveals high-conductivity anomaly, whereas seismic tomography suggests high-velocity structure. This could be an indication of the processes that act differently on conductivity and seismic velocities. A weak correlation between high (low) conductivities and low (high) velocities may be attributed, for example, to the water effect (Koyama *et al.* 2006). However, we have to state that more work is still needed to ascertain the full robustness of the features observed in our 3-D EM images.

6 CONCLUSIONS AND OUTLOOK

6.1 Conclusions

A novel 3-D inversion tool for global EM studies in the frequency domain has been developed by Kuvshinov & Semenov (2012) and verified with synthetic data. In this paper the developed 3-D inverse solution has been applied to real ground-based geomagnetic data. The goal was to obtain 3-D images of the electrical conductivity distribution in the mantle at depths between 400 and 1600 km. As a first step we collected and analysed very long time-series (up to 51 years; 1957–2007) of hourly means of three components of the geomagnetic field from 281 geomagnetic observatories. Special

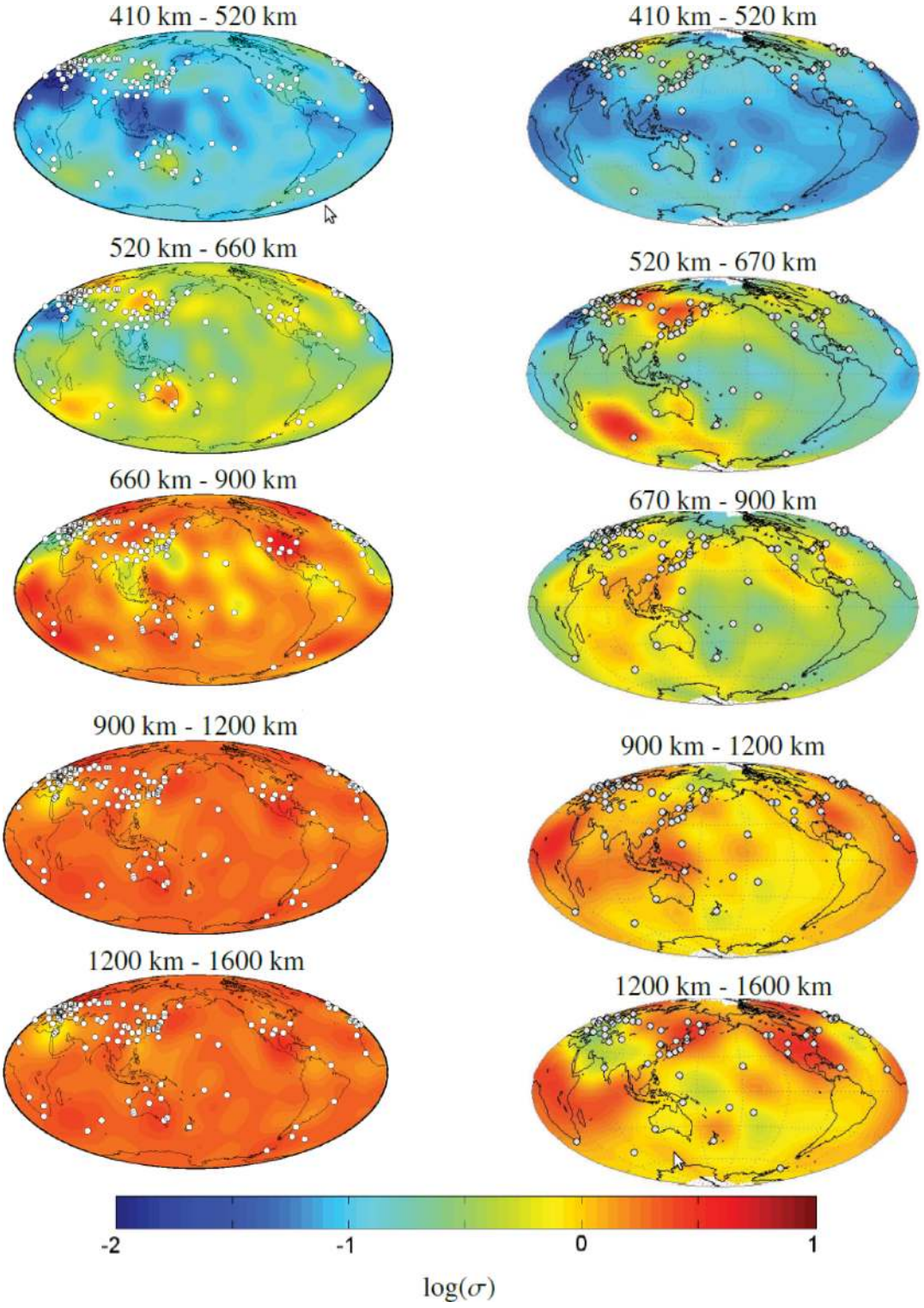

Figure 33. Comparison of our results (left-hand plots) with results from Kelbert *et al.* (2009) study (right-hand plots).

attention was given to data processing to obtain unbiased *C*-responses with trustworthy estimates of experimental errors in the period range from 2.9 to 104.2 d.

After careful inspection of the obtained *C*-responses we chose the data from 119 observatories for the further analysis. Squared coherency was used as a main quality indicator to detect (and then to exclude from consideration) observatories with large noise-to-signal ratios. During this analysis we found that—along with the *C*-responses from high-latitude observatories (geomagnetic latitudes higher than 58°)—the *C*-responses from all low-latitude observatories (geomagnetic latitudes below 11°) also have very low squared coherencies, and thus cannot be used for global induction studies.

We found that the *C*-responses from the selected 119 mid-latitude observatories show a huge variability both in real and imaginary

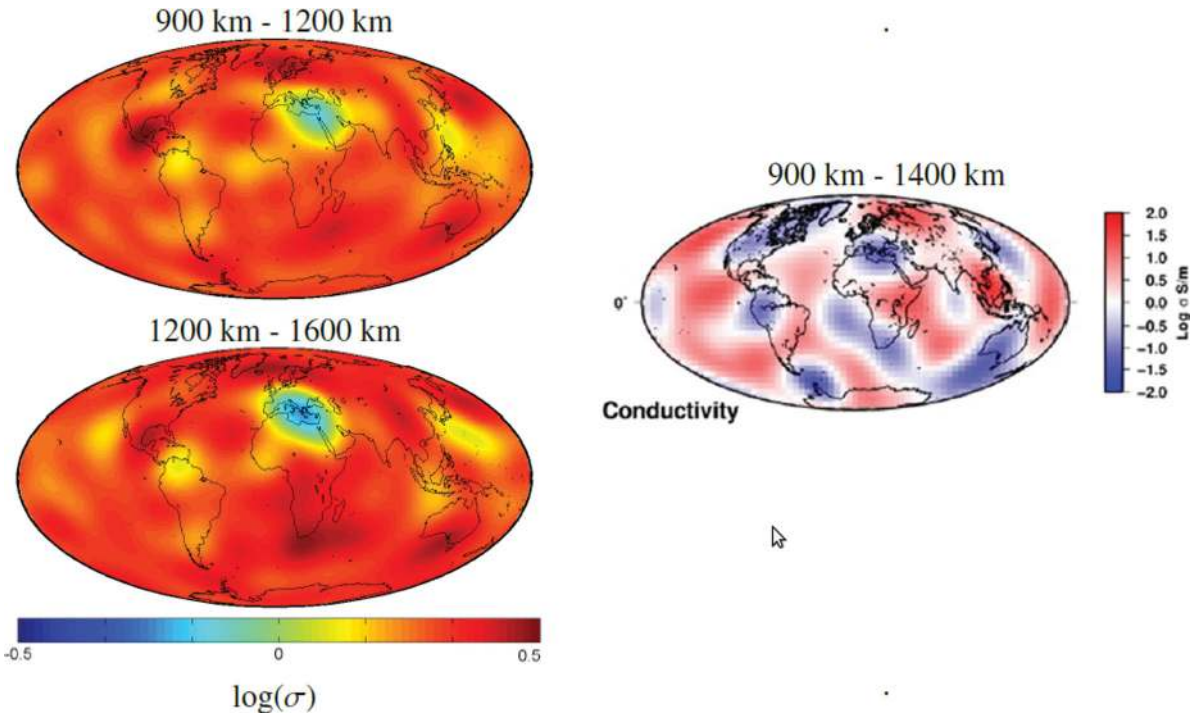

Figure 34. Comparison of our results (left-hand plots) with Tarits & Mandea (2010) study (right-hand plot).

parts, and we investigated to what extent the ocean effect can explain such a scatter. By performing the systematic model calculations we come to the following conclusions. (1) The variability due to the ocean effect is substantial, especially at shorter periods, and it is seen for periods up to 40 d or so. (2) The imaginary part of the *C*-responses is to a larger extent (compared with the real part) influenced by the oceans. (3) Two types of anomalous *C*-response behaviour associated with the ocean effect can be distinguished. The first type is characterized by substantial increase in both real and imaginary parts towards shorter periods. In addition, at small periods (of our period range) the imaginary part becomes positive. Such behaviour of the *C*-responses is not compatible with any 1-D conductivity structure, which always has a negative imaginary part (for adopted $e^{i\omega t}$ time-dependence convention), and a descending real part with decreasing period. Three end-member observatories, showing maximum ocean effect of this type, are KOU (Kourou, French Guiana), VSS (Vassouras, Brasil), and HER (Hermanus, South Africa). The second type of anomalous behaviour is apparent as an excessive (compared with a 1-D case) decrease in both real and imaginary parts of the *C*-responses with decreasing period. Three observatories, showing maximum ocean effect of this type, are the Japanese observatories SSO (Simosato), HTY (Hatizyo) and KNY (Kanoya). (4) In order to accurately reproduce the ocean effect, a lateral resolution of $1^\circ \times 1^\circ$ of the conductance distribution is needed. Note that from the point of view of practicality such a resolution in the case of 3-D inversion still requires prohibitively high computational loads, and the applied correction scheme to account for the ocean effect is only approximate. (5) The ocean effect alone does not explain the whole variability of the observed *C*-responses, in particular the variability observed in the real part.

We also found that part of the variability in the real part of the *C*-responses is due to the auroral effect, which manifests itself as an excessive decrease of the real part at shorter periods. In addition to the observation of Fujii & Schultz (2002) that the influence of the auroral current system can be traced in *C*-responses to a geomagnetic latitude of 40° *globally*, we also found that the auroral effect in the *C*-responses reveals strong longitudinal variability, at least in the Northern Hemisphere. Moreover, as the auroral effect is seen as the decay of the real part of the *C*-responses towards higher latitudes, we clearly showed that the latitudinal pattern of the decay varies with the region and that this pattern persists in the whole period range. Europe appears to be the region with smallest degree of distortion compared with North America and northern Asia. It is interesting that the imaginary part of the *C*-responses is weakly affected by the auroral source, thus confirming the fact that in the considered period range the EM induction from the auroral electrojet is small (due to the small-scale spatial pattern of this source). Assuming the weak dependence of the auroral signals on the Earth's conductivity, and the longitudinal variability of the auroral effect, we developed an approximate scheme to correct the experimental *C*-responses for this effect.

With these developments and findings in mind we performed a number of regularized 3-D inversions of our experimental data to detect robust features in the recovered 3-D conductivity images. The proper choice of the regularization parameter (for each inversion run) was based on the standard L-curve formalism.

Although differing in details, all our 3-D inversions reveal a substantial level of lateral heterogeneity in the mantle at the depths between 410 and 1600 km. Conductivity values vary laterally by more than one order of magnitude between resistive and conductive regions. The maximum lateral variations of the conductivity have been detected in the layer at depths between 670 and 900 km. In the layers below (between 900 and 1600 km) the overall tendency is that lateral conductivity variations diminish in magnitude with depth. As expected, polar, equatorial and oceanic regions, where we lack data, are poorly resolved. It is believed that the forthcoming *Swarm* geomagnetic satellite mission (Olsen *et al.* 2010)

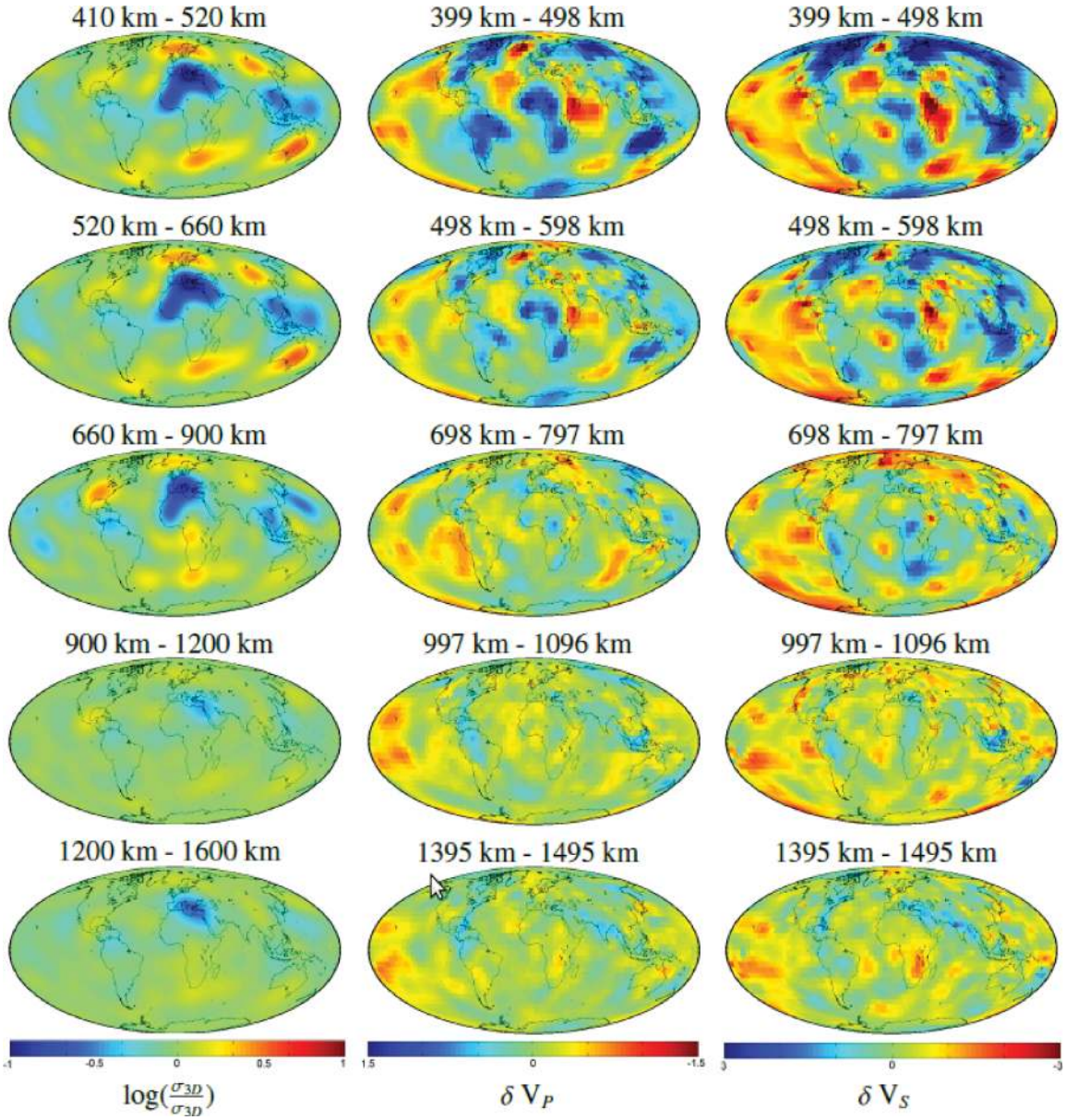

Figure 35. Comparison of our results (left-hand column of plots) with the *P*-wave (middle column of plots) and *S*-wave (right-hand column of plots) distributions from Della Mora *et al.* (2011).

will improve the situation, providing a much better spatial data coverage.

By comparing our global 3-D results with the results of independent global and semi-global 3-D conductivity studies, we conclude that 3-D conductivity mantle models produced so far are preliminary as different groups obtain disparate results, thus complicating quantitative comparison with seismic tomography or/and geodynamic models. The present discrepancy is most probably due to: (1) strong non-uniqueness of the inverse problem arising from spatial sparsity and irregularity of data distribution, variable data quality and limited period range; (2) different data sets; (3) different inversion settings, including forward problem gridding, model parametrization, form of regularization term employed and choice of regularization parameter; (4) inconsistency of external field models, for example, improper account/correction for the auroral effect and/or ignoring asymmetric part of the ring current, and (5) possible inaccuracy in forward and inverse solutions.

In spite of this, our 3-D study and most other 3-D studies reveal at least two robust features: (1) reduced conductivity beneath southern Europe and northern Africa, and (2) enhanced conductivity in northeastern China.

6.2 Outlook for future studies

6.2.1 Extending the data for global 3-D EM inversions

While the data from geomagnetic satellite missions are believed to be very important, we think that the major input for 3-D conductivity studies will still come from ground-based data. In spite of continuing efforts there are still large gaps in the ground-based network, especially in oceanic areas and in the Southern Hemisphere. In the last decade a number of geomagnetic observatory projects have been initiated to improve the coverage by long-term measurements in those regions. From 2007 GFZ (Helmholtz-Zentrum

Potsdam) has been operating an observatory in the South Atlantic Ocean on St Helene Island (Korte *et al.* 2009). In 2008, a new observatory on Easter Island (South Pacific Ocean) was installed by Institut de Physique du Globe de Paris (France) and Direccion Meteorologica de Chile (Chulliat *et al.* 2009). Since 2009 the National Space Institute at the Technical University of Denmark has been running an observatory on Tristan da Cuhna Island also located in the South Atlantic Ocean (Matzka *et al.* 2009). The Institute of Geophysics, ETH Zurich (Switzerland), is in the process of installing and running two observatories in the Indian Ocean—on Gan island, Maldives (in cooperation with Maldives Meteorological Service and National Geophysical Research Institute, Hyderabad, India) and on Cocos Island (in cooperation with Geoscience Australia).

A few long-term geomagnetic stations have been installed by Ocean Hemisphere Research Center (OHRC) of ERI (Shimizu & Utada 1999) in the Pacific Ocean. Five stations, at Majuro (Marshall Islands), Pohnpei (Micronesia), Muntinlupa (Philippines), Atele (Tonga), Marcus Island (Japan), are running and OHRC plans to continue observations at these sites.

The irregular distribution of the land/island geomagnetic observatories is improved by extending the geomagnetic observatories to the seafloor. Toh *et al.* (2006, 2010) reported on the operation of two long-term seafloor stations. One station has been operating in the North West Pacific since 2001 and the other has been operating in the West Philippine Basin since 2006. Their seafloor data consist of the geomagnetic vector and scalar field measurements along with attitude measurements for both orientation and tilt. In addition, horizontal components of the electric field are measured, thus allowing for long period MT sounding.

Note that long period electric field measurements more often complement magnetic field observations. During 2001–2003 MT data have been collected at the positions of 11 geomagnetic observatories situated within a few hundred kilometres along the southwest margin of the East European Craton (Semenov *et al.* 2008). Long period MT measurements have been conducted at seven backbone MT stations across North America in the frame of Earthscope project (Schultz 2010). These data are very relevant for global induction studies since the use of electric fields allows us to obtain C-responses at periods shorter than a few days and thus to provide information on conductivities at depths shallower than 400 km. Another merit of the MT technique is that it works in regions where the GDS method fails. For example, MT measurements might be helpful in the vicinity of the geomagnetic equator where B_r of magnetospheric origin is close to zero thus preventing the use of the GDS method. High latitudes are also favourable for MT experiments since in these regions the GDS method also fails to work due to the fact that here the source structure is completely different from the P_1^0 structure (that is assumed by default in the GDS method). Finally, use of the electric field allows us to probe relatively resistive structures in the mantle that is not readily possible using magnetic observations only.

In addition to local MT observations, variations of the voltage differences measured with the use of the retired transoceanic submarine cables provide unique information in oceanic regions (Lizarralde *et al.* 1995; Utada *et al.* 2003, among others). Note that there exist already first successful examples of 3-D semi-global joint analysis of the data from geomagnetic observatories and trans-Pacific cables (*cf.* Koyama *et al.* 2006; Shimizu *et al.* 2010b). In summary, we believe that complementing the existing data with the above-mentioned data should improve the reliability and resolution of the global 3-D images of mantle electrical conductivity.

Lastly, the analysis of forthcoming satellite data from *Swarm* or joint analysis of satellite and ground-based data should enhance the capability to detect lateral conductivity variations, especially in the vast oceanic regions where the ground-based data are still rare. However, the 3-D EM inversion of satellite data is a challenging problem since satellite data analysis is more difficult compared to observatory data, because satellites move typically with a speed of 7–8 $\mathrm{km\,s^{-1}}$ and thus measure a mixture of temporal and spatial changes of the magnetic field. A review of the approaches for induction studies from space is given by Kuvshinov (2012).

6.2.2 Proper account/correction for the auroral effect

Our attempt to correct for the auroral effect in 3-D inversion of ground-based C-responses cannot be said to be fully successful. Artefacts are still present in global 3-D conductivity images at polar latitudes. A future goal would be to understand the physical processes occurring in the auroral regions to obtain quantitative models of the polar electrojets and incorporate these into global 3-D EM inversion schemes. Alternatively one can use at higher altitudes only imaginary part of the responses which is in lesser extent influenced by auroral effect.

6.2.3 Further developments of our global 3-D EM inversion solution

Our experience with the development of global 3-D EM inversion and its implementation to real data allows us to formulate some possible directions for how this can be improved and extended. These directions are as follows.

The forward problem gridding of $3^\circ \times 3^\circ$ used during 3-D inversion is most probably not enough to account accurately for the ocean effect. Our attempt to run inversion on a dense grid of $1^\circ \times 1^\circ$ were computationally prohibitive. We also tried to correct the data for the ocean effect using dense gridding, but found that such correction only slightly influenced the results. Modification of the forward modelling scheme to allow for different lateral gridding in surface (denser grid) and deeper (coarser grid) layers could resolve this problem.

In existing inversion solution the volume cells, where the conductivities are searched for, are assumed to cover uniformly (in lateral directions) the inverse volume. More flexible options of the inverse volume parametrization seems to be more appropriate for ground-based data. For example, discretization of the inverse volume can be made denser beneath the regions with better data coverage and sparser in the regions with no data. However, this will require development of numerical algorithm(s) to perform it in the most consistent way. Such flexibility in the model parametrization will also require elaboration of new regularization schemes which will account for this spatially non-uniform parametrization.

If long period MT responses and the voltage difference will be included in the interpretation, one has to derive the formulae for the adjoint sources, which are needed to calculate efficiently the data misfit gradient. This can be done by applying a formalism developed by Pankratov & Kuvshinov (2010).

Despite a certain success of 3-D EM analysis of global induction data the quantification of the model resolution is still deficient. Until now the resolution studies are based on synthetic inversions for specific (checkerboard) input structures. However, one can gain important information about resolution and the trade-offs between model parameters from the Hessian matrix (matrix of second derivatives

of the misfit functional with respect to these parameters). Recently, Fichtner & Trampert (2011) presented an extension of the adjoint method that allows them to compute efficiently the second derivatives of seismic data misfit functionals. Perhaps this approach can be adopted for EM studies, and thus would serve as a prelude to the development of quantitative resolution analyses.

6.2.4 Implementation of the alternative approach to global 3-D EM inversion

The approach discussed in this paper is based on an assumption that the spatial structure of the magnetospheric ring current—which is responsible for geomagnetic variations of our interest—is described by first zonal harmonic in geomagnetic coordinate system. Namely this assumption allows us to use the *C*-response concept. However it is well recognized now that the geometry of real magnetospheric ring current can significantly deviate from this simple model (*cf*. Olsen & Kuvshinov 2004; Balasis & Egbert 2006, among others). Thus there is strong need for the methodologies that allow for working in consistent manner with the data generated by the sources of arbitrary geometry. One promising approach has been proposed in Fainberg *et al.* (1990). Two basic ideas behind the method are: (1) one has to work with the fields (more exactly with the time spectra of the fields) rather than with the responses, and (2) one has to determine simultaneously the parameters describing the source and conductivity distribution in the Earth. Note that with the ultimate goal of working with the 3-D conductivity models, this method has been so far applied to estimate 1-D conductivity distribution in the middle and lower mantle (Singer *et al.* 1993).

ACKNOWLEDGMENTS

Authors express their gratitude to the staff of the geomagnetic observatories who has been collecting and distributing the data. Authors thank Amir Khan and Chris Finlay for overall comments as well as help with improving the English presentation of the paper. This work has been supported by ETH grant no. 0-20423-07, and in part by European Space Agency through ESTEC contracts no. 20944/07/NL/JA and no. 22656/09/NL/FF.

REFERENCES

Balasis, G. & Egbert, G., 2006. Empirical orthogonal function analysis of magnetic observatory data: Further evidence for non-axisymmetric magnetospheric sources for satellite induction studies, *Geophys. Res. Lett.,* **33,** L11311, doi:10.1029/2006GL025721.

Banks, R., 1969. Geomagnetic variations and the electrical conductivity of the upper mantle, *Geophys. J. R. astr. Soc.,* **17,** 457–487.

Becker, T. & Boschi, L., 2002. A comparison of tomographic and geodynamic mantle models, *Geochem. Geophys. Geosyst.,* **3,** 1003, doi:10.129/2001GC000168.

Chave, D.A. & Thomson, D., 1989. Some comments on magnetotelluric response function estimation, *J. geophys. Res.*, **94,** 14 215–14 225.

Chulliat, A., Lalanne, X., Gaya-Peque, L., Truong, F. & Savary, J., 2009. The new Easter Island magnetic observatory, in *Proceedings of the XIIIth IAGA Workshop on Geomagnetic Observatory Instruments, Data Acquisition and Processing (Love, J.J.),* [US Geological Survey Open-File Report 20091, 20091226, pp. 47–53.

Della Mora, S., Boschi, L., Tackley, P., Nakagawa, T. & Giardini, D., 2011. Low seismic resolution cannot explain S/P decorrelation in the lower mantle, *Geophys. Res. Lett.,* **38,** L12303, doi:10.1029/2011GL047559.

Dziewonski, A. & Anderson, D., 1981. Preliminary reference Earth model, *Phys. Earth planet Inter.,* **25,** 297–356.

Efron, B., 1982. *The Jackknife, the Bootstrap, and other Resampling Plans*, Society for Industrial and Applied Mathematics, Philadelphia, PA.

Egbert, G., Booker, J. & Schultz, A., 1992. Very long period magnetotellurics at Tucson observatory: implications for mantle conductivity, *J. geophys. Res.,* **97,** 15 099–15 112.

Everett, M., Constable, S. & Constable, C., 2003. Effects of near-surface conductance on global satellite induction responses, *Geophys. J. Int.,* **153,** 277–286.

Faccena, C., Jolivet, L., Piromallo, C. & Morelli, A., 2003. Subduction and the depth of convection in the Mediterranean mantle, *J. geophys. Res.,* **108**(B2), 2099, doi:10.1029/2001JB001690.

Fainberg, E., Kuvshinov, A., Mishina, L. & Singer, B., 1990. The new approach to global deep soundings, *Pure Appl. Geophys.,* **134,** 527–531.

Fichtner, A. & Trampert, J., 2011. Hessian kernels of seismic data functionals based upon adjoint techniques, *Geophys. J. Int.,* **185,** 775–798.

Finlay, C., Maus, S., Beggan, C., Hamoudi, M., Lowes, F., Olsen, N. & Thebault, E., 2010. Evaluation of candidate geomagnetic field models for IGRF-11, *Earth Planets Space,* **62,** 787–804.

Fujii, I. & Schultz, A., 2002. The 3-D electromagnetic response of the Earth to the ring current and auroral oval excitation, *Geophys. J. Int.,* **151,** 689–709.

Fukao, Y., Widiyantoro, S. & Obayashi, M., 2001. Stagnant slabs in the upper and lower mantle transition region, *Rev. Geophys.,* **39,** 291–323.

Fukao, Y., Koyama, T., Obayashi, M. & Utada, H., 2004. Trans-Pacific temperature field in the mantle transition region derived from seismic and electromagnetic tomography, *Earth planet. Sci. Lett.,* **217,** 425–434.

Gamble, T., Clarke, J. & Goubau, W., 1979. Magnetotellurics with a remote magnetic reference, *Geophysics,* **4,** 53–68.

Grand, S., 1994. Mantle shear structure beneath Americas and surrounding oceans, *J. geophys. Res.,* **99,** 11 591–11 621.

Hansen, P., 1992. Analysis of discrete ill-posed problems by means of the L-curve, *SIAM Rev.,* **34,** 561–580.

Helffrich, G. & Wood, B., 2001. The Earth's mantle, *Nature,* **412,** 507–507, doi:10.1038/35087500.

Huber, P., 1981. *Robust Statistics*, Wiley, New York, NY.

Ichiki, M., Uyeshima, M., Utada, H., Guoze, Z., Ji, T. & Mingzhi, M., 2001. Upper mantle conductivity structure of the back-arc region beneath north-eastern China., *Geophys. Res. Lett.,* **28,** 3773–3776.

Jones, A., Evans, R. & Eaton, D., 2009. Velocity-conductivity relationships for mantle minerals assemblages in Archean cratonic lithosphere based on review of laboratory data and Hashin-Shtrikman extremal bounds, *Lithos,* **131,** doi:10.1016/j.lithos.2008.10.014.

Kelbert, A., Schultz, A. & Egbert, G., 2009. Global electromagnetic induction constraints on transition-zone water content variations, *Nature,* **460,** 1003–1007.

Khan, A., Kuvshinov, A. & Semenov, A., 2011. On the heterogeneous electrical conductivity structure of the Earth's mantle with implications for transition zone water content, *J. geophys. Res.,* **116,** B01103, doi:10.1029/2010JB007458.

Korte, M., Mandea, M., Linthe, H., Hemshorn, A., Kotze, P. & Ricaldi, E., 2009. New geomagnetic field observations in the South Atlantic anomaly region, *Ann. Geophys.,* **52,** 65–82.

Koyama, T., 2001. A study on the electrical conductivity of the mantle by voltage measurements of submarine cables, *PhD thesis*, University of Tokyo.

Koyama, T., Shimizu, H., Utada, H., Ichiki, M., Ohtani, E. & Hae, R., 2006. Water content in the mantle transition zone beneath the North Pacific derived from the electrical conductivity anomaly, *Am. geophys. Un. Geophys. Monogr. Ser.,* **168,** 171–179.

Kuo, F. & Kaiser, J., 1966. *System Analysis by Digital Computer*, Wiley, New York, NY.

Kuvshinov, A., 2008. 3-D global induction in the oceans and solid Earth: recent progress in modeling magnetic and electric fields from sources of magnetospheric, ionospheric and oceanic origin, *Surv. Geophys.,* **29,** 139–186, doi:10.1007/s10712-008-9045-z.

Kuvshinov, A., 2012. Deep electromagnetic studies from land, sea, and space: progress status in the past 10 years, *Surv. Geophys.,* **33,** 169–209, doi:10.1007/s10712-011-9118-2.

Kuvshinov, A. & Olsen, N., 2006. A global model of mantle conductivity derived from 5 years of CHAMP, Ørsted, and SAC-C magnetic data, *Geophys. Res. Lett.,* **33,** L18301, doi:10.1029/2006GL027083.

Kuvshinov, A. & Semenov, A., 2012. Global 3-D imaging of mantle electrical conductivity based on inversion of observatory *C*-responses—I. An approach and its verification, *Geophys. J. Int.,* **189,** 1335–1352.

Kuvshinov, A.V., Olsen, N., Avdeev, D.B. & Pankratov, O.V., 2002. Electromagnetic induction in the oceans and the anomalous behaviour of coastal *C*-responses for periods up to 20 days, *Geophys. Res. Lett.,* **29,** 12, doi:10.1029/2001GL014409.

Laske, G. & Masters, G., 1997. A global digital map of sediment thickness, *EOS, Trans. Am. geophys. Un.,* **78,** F483.

Lizarralde, D., Chave, A., Hirth, G. & Schultz, A., 1995. Long period magnetotelluric study using Hawaii-to-California submarine cable data: implications for mantle conductivity, *J. geophys. Res.,* **100,** 17 873–17 884.

Manoj, C., Kuvshinov, A., Maus, S. & Lühr, H., 2006. Ocean circulation generated magnetic signals, *Earth Planets Space,* **58,** 429–439.

Matzka, J., Olsen, N., Fox Maule, C., Pedersen, L., Berarducci, A. & Macmillan, S., 2009. Geomagnetic observations on Tristan da Cuhna, South Atlantic ocean, *Ann. Geophys.,* **52,** 97–105.

Megnin, C. & Romanowicz, B., 2000. The three-dimensional shear velocity structure of the mantle from the inversion of body, surface and higher mode waveforms, *Geophys. J. Int.,* **143,** 709–728.

Neal, S.L., Mackie, R.L., Larsen, J.C. & Schultz, A., 2000. Variations in the electrical conductivity of the upper mantle beneath North America and the Pacific Ocean, *J. geophys. Res.,* **105,** 8229–8242.

Obayashi, M., Sugioka, H., Yoshimitsu, H. & Fukao, Y., 2006. High temperature anomalies oceanward of subducting slabs at the 410 km discontinuity, *Earth planet. Sci. Lett.,* **243,** 149–158.

Olsen, N., 1998. The electrical conductivity of the mantle beneath Europe derived from *C*-responses from 3 to 720 hr, *Geophys. J. Int.,* **133,** 298–308.

Olsen, N. & Kuvshinov, A., 2004. Modelling the ocean effect of geomagnetic storms, *Earth Planets Space,* **56,** 525–530.

Olsen, N., Hulot, G. & Sabaka, T., 2010. Sources of geomagnetic field and the modern data that enable their investigation, in *Handbook of Geomathematics*, pp. 106–124, eds Freeden, W., Nashed, M.Z. & Sonar, T., Springer, Heidelberg.

Pankratov, O. & Kuvshinov, A., 2010. General formalism for the efficient calculation of derivatives of EM frequency domain responses and derivatives of the misfit, *Geophys. J. Int.,* **181,** 229–249.

Roberts, R., 1984. The long-period electromagnetic response of the Earth, *Geophys. J. R. astr. Soc.,* **78,** 547–572.

Romanowicz, B., 2003. Global mantle tomography: progress status in the past 10 years, *Ann. Rev. Earth Planet,* **31,** 303–328.

Schmucker, U., 1999. A spherical harmonic analysis of solar daily variations in the years 1964-1965: response estimates and source fields for global induction—II. Results, *Geophys. J. Int.,* **136,** 455–476.

Schultz, A., 2010. EMScope: a continental scale magnetotelluric observatory and data discovery resource, *Data Sci. J.,* **8,** IGY6–IGY20.

Schultz, A. & Larsen, J., 1987. On the electrical conductivity of the mid-mantle: I. Calculation of equivalent scalar magnetotelluric response functions, *Geophys. J. Int.,* **88**(3), 733–761.

Semenov, V., Pek, J., Adam, A., Jozwiak, W., Ladanyvskyy, B., Logvinov, I., Pushkarev, P. & Vozar, J., 2008. Electrical structure of the upper mantle beneath central Europe: results of the CEMES project, *Acta Geophys.,* **56,** 957–981.

Shankland, T., Peyronneau, J. & Poirer, J., 1993. Electrical conductivity of the Earth's lower mantle, *Nature,* **366,** 453–455.

Shimizu, H. & Utada, H., 1999. Ocean hemisphere geomagnetic network: its instrumental design and perspective for long-term geomagnetic observations in the Pacific, *Earth Planets Space,* **51,** 917–932.

Shimizu, H., Koyama, T., Baba, K. & Utada, H., 2010a. Revised 1-D mantle electrical conductivity structure beneath the North pacific, *Geophys. J. Int.,* **180,** 1030–1048.

Shimizu, H., Utada, H., Baba, K., Koyama, T., Obayashi, M. & Fukao, Y., 2010b. Three-dimensional imaging of electrical conductivity in the mantle transition zone beneath the North Pacific ocean by a semi-global induction study, *Phys. Earth planet. Int,* **183,** 252–269, doi:10.1016/j.pepi.2010.01.010.

Singer, B., Kuvshinov, A., Mishina, L. & Fainberg, E., 1993. Global geomagnetic sounding: new methodology and results, *Izvestiya, Phys. solid Earth,* **29,** 35–43.

Tarits, P. & Mandea, M., 2010. The heterogeneous electrical conductivity structure of the lower mantle, *Phys. Earth Planet. Int.,* **183,** 115–125, doi:10.1016/j.pepi.2010.08.002.

Tarits, P., Hautot, S. & Perrier, F., 2004. Water in the mantle: results from electrical conductivity beneath the French Alps, *Geophys. Res. Lett.,* **31,** L06612, doi:10.1029/2003GL019277.

Toh, H., Hamano, Y. & Ichiki, M., 2006. Long-term seafloor geomagnetic station in the Northwest Pacific: a possible candidate for a seafloor geomagnetic observatory, *Earth Planets Space,* **58,** 697–705.

Toh, H., Hamano, Y., Goto, Y. & Utada, H., 2010. Long-term seafloor electromagnetic observation in the northwest Pacific may detect the vector geomagnetic secular variation, *Data Sci. J.,* **9,** IGY100–IGY109.

Utada, H., Koyama, T., Shimizu, H. & Chave, A., 2003. A semi-global reference model for electrical conductivity in the mid-mantle beneath the North Pacific region, *Geophys. Res. Lett.,* **30,** 1194, doi:10.1029/2002GL016092.

Utada, H., Koyama, T., Obayashi, M. & Fukao, Y., 2009. A joint interpretation of electromagnetic and seismic tomography models suggests the mantle transition zone below Europe is dry, *Earth planet Sci. Lett.,* **281,** 249–257.

van der Hilst, R., Engdal, R., Spakman, W. & Nolet, G., 1991. Tomographic imaging of subducted lithosphere below northwest Pacific island arcs, *Nature,* **353,** 37–43.

Verhoeven, O. *et al.*, 2009. Constraints on thermal state and composition of the Earth's lower mantle from electrical impedances and seismic data, *J. geophys. Res.,* **114,** B03302, doi:10.1029/2008JB005678.

Weidelt, P., 1972. The inverse problem of geomagnetic induction, *Z. Geophys.,* **38,** 257–289.